

**Applications of Infrared Fibers in Temperature Sensing**

by

**Amy L. Matthews**

Thesis submitted to the Faculty of the  
Virginia Polytechnic Institute and State University  
in partial fulfillment of the requirements for the degree of  
Master of Science  
in  
Electrical Engineering

**APPROVED:**

---

**Richard O. Claus, Chairman**

---

**Ronald J. Pieper**

---

**John C. McKeeman**

**June, 1988**

**Blacksburg, Virginia**

# Applications of Infrared Fibers in Temperature Sensing

by

Amy L. Matthews

Richard O. Claus, Chairman

Electrical Engineering

(ABSTRACT)

As attenuation in silica based fibers approaches its ultimate theoretical limit, investigation is in progress to develop new materials which exhibit lower losses than silica. These bulk materials could then be used to fabricate ultralow loss optical fibers which operate farther out in the infrared than do silica fibers. Such infrared fibers could be used in long, repeaterless telecommunications links, the transmission of  $CO$  and  $CO_2$  laser power, and in several sensing mechanisms. This thesis presents an overview of these new fibers and how they can be applied in noncontact temperature measurement. Fiber optic temperature sensing is thus reviewed, and an optical fiber pyrometer is discussed.

# Acknowledgements

Many sincere thanks go to Rick Claus, my graduate advisor, for his patience, support, and encouraging smiles.

Thanks to both Ron Pieper, who was always willing to take the time to answer my questions and help me out, and John McKeeman for being members of my committee.

The students and staff of the Fiber & Electro-Optics Research Center have each influenced, advised, and supported me in their own ways. I value their friendships. Thank you all; particularly .

Special thanks to , for making my last few months at Virginia Tech such happy ones.

And finally, I want to thank Mom and Daddy, , , , , , , and . Not to mention , , , , , and . Knowing you were all out there always helped. In many ways on many days.

# Table of Contents

<b>1.0 Introduction</b> .....	<b>1</b>
<b>2.0 Principles of Silica-Based Optical Fibers</b> .....	<b>4</b>
2.1 Basic Parameters .....	4
2.2 Fiber Classification .....	8
2.3 Attenuation .....	10
2.3.1 Absorption Loss .....	10
2.3.2 Scattering Loss .....	15
2.3.3 Radiative Losses .....	16
2.4 Dispersion .....	18
2.4.1 Material Dispersion .....	19
2.4.2 Waveguide Dispersion .....	20
2.4.3 Intermodal Dispersion .....	23
2.5 Fiber Fabrication Methods .....	24
2.5.1 Direct Melt Methods .....	24
2.5.2 Vapor Phase Oxidation Methods .....	26

<b>3.0 Nonsilica-Based Infrared Fibers</b> .....	<b>30</b>
3.1 Fibers for the Near Infrared .....	31
3.2 Fibers for the Mid Infrared .....	32
3.2.1 Halides .....	32
3.2.2 Heavy Metal Oxides .....	34
3.3 Fibers for the Far Infrared .....	35
3.3.1 Chalcogenides .....	35
3.3.2 Crystalline Materials .....	36
3.4 Fabrication Methods .....	38
3.4.1 Fluoride Glass Fibers .....	38
3.4.2 Heavy Metal Oxide Fibers .....	43
3.4.3 Chalcogenide Fibers .....	44
3.4.4 Crystalline Fibers .....	46
3.5 Comments on Infrared Fibers .....	47
3.6 An Application .....	49
<b>4.0 Fiber Optic Temperature Sensors</b> .....	<b>50</b>
4.1 Interferometric Sensors .....	51
4.1.1 Mach-Zehnder Interferometers .....	52
4.1.2 Michelson Interferometer .....	54
4.1.3 Wavelength-Modulated Interferometers .....	56
4.1.4 Polarimetric Interferometers .....	58
4.1.5 Fabry-Perot Interferometers .....	62
4.1.6 Cross-talk Interferometer .....	63
4.2 Fluorescence-Based Temperature Sensors .....	65
4.3 Evanescent Field Absorption Sensor .....	68
4.4 OTDR Temperature Sensing .....	70
4.4.1 Liquid-Core Fiber Distributed Temperature Sensor .....	70

4.4.2 Raman Ratio Temperature Sensing .....	73
4.5 A Reflectometer to Sense Temperature .....	77
4.6 Optical Fiber Pyrometers .....	79
4.7 Summary .....	81
<b>5.0 Pyrometry: Theory and Experiment .....</b>	<b>82</b>
5.1 Theory .....	82
5.2 Experiment .....	88
<b>6.0 Future Work and Conclusions .....</b>	<b>100</b>
6.1 Future Work .....	100
6.2 Conclusions .....	101
<b>References .....</b>	<b>103</b>
<b>Vita .....</b>	<b>108</b>

# List of Illustrations

Figure 1. Reflection and Refraction in an Optical Fiber [2] .....	6
Figure 2. The Numerical Aperture of an Optical Fiber [2] .....	7
Figure 3. Classification of Optical Fibers .....	11
Figure 4. Attenuation Curve for Silica Fiber [8] .....	13
Figure 5. Attenuation due to (a) Absorption (b) Scattering [2] .....	17
Figure 6. Material Dispersion Curve [8] .....	21
Figure 7. Apparatus for Direct-Melt Methods .....	25
Figure 8. Apparatus for Vapor Phase Oxidation Methods .....	28
Figure 9. Fluoride Fiber Fabrication Techniques .....	40
Figure 10. Fluoride Fiber Fabrication Techniques .....	42
Figure 11. Fabrication Methods for Chalcogenides and Crystalline Fibers .....	45
Figure 12. A Mach-Zehnder Interferometer [35] .....	53
Figure 13. A Michelson Interferometer [39] .....	55
Figure 14. A Wavelength-Modulated Interferometer [41] .....	57
Figure 15. A Polarimetric Interferometer [42] .....	61
Figure 16. A Fluorescence-Based Temperature Sensor [44] .....	66
Figure 17. An Evanescent Field Absorption Sensor [45] .....	69
Figure 18. A Liquid-Core OTDR Sensing System [46] .....	72
Figure 19. Raman OTDR Temperature Sensing Systems [47] .....	76

Figure 20. A Reflectometer to Sense Temperature [50] .....	78
Figure 21. Blackbody Radiation Curves [52] .....	84
Figure 22. Filter Options .....	90
Figure 23. Filter Options .....	91
Figure 24. Filter Options .....	92
Figure 25. Drop Tube Instrumentation .....	93
Figure 26. Experimental Set-up .....	95
Figure 27. Power Collected, First Trial .....	97
Figure 28. Power Collected, Second Trial .....	98
Figure 29. Ratio of Power Collected, First and Second Trials .....	99

# 1.0 Introduction

Fiber optics for communications, instrumentation, and sensing is a burgeoning technology. Rapid advances in each of these areas are leading to new directions and new applications for optical fibers.

One such direction includes transmissive materials for the infrared region of the electromagnetic spectrum. Typical silica-based fibers operate up to 1550 nm and have losses as low as 0.2 dB/km. New fibers, based on materials other than silica, will be capable of operation into the far infrared. Theoretically, long-wavelength optical fibers have been predicted to exhibit loss down to  $10^{-2}$  to  $10^{-3}$  dB/km [1]. This very low loss makes infrared fibers excellent candidates for long-haul repeaterless communication links, short length power transmission, and infrared sensors.

The potential use of infrared-transmitting optical fibers in multi-wavelength pyrometers is the main motivation for this thesis. Multi-wavelength pyrometers are necessary in high temperature and remote sensing environments. Examples of such environments are the processing of aluminum and steel, hot aerospace structures, and drop tubes.

In aluminum and steel rolling mills, the measurement of temperature at various positions along the system is most important. This is because a number of processes, both the "internal" material processes such as phase transitions, for example, and the "external" processes such as forming and extruding, are inextricably linked to the temperature of the metal. An accurate measure of temperature in such systems would optimize the fabrication process and save both machine wear and the energy needed to achieve material temperature.

In "hot" aerospace structures, the motivation is that the leading edges of supersonic aircraft as well as the engines of many aircraft operate at extremely high temperatures. The accurate measurement of temperature in both of these cases is important. In the hot aerospace structure case, one idea that has been proposed is to pump liquids through (and maybe out of) the surfaces to affect "transpiration-cooled" surfaces (i.e., the airplanes sweat). Knowledge of temperature, and in particular distributed temperature, is needed to determine how much liquid, how much cooling, and how much sweat is needed; that is, needed to cool the structure to a reasonable temperature.

Regarding the drop tube case, we propose a "many fiber - single detector" system. This idea is attractive because it saves the cost of additional detectors, as well as the size of them. In a twenty port tube, for example, nineteen "extra" detectors could cost an unnecessary \$50,000 - \$500,000.

Although the basics for silica-based and nonsilica-based optical fibers are similar, the two types of fibers also differ in several respects. Therefore, Chapter 2 will review the silica-based fiber, and Chapter 3 will extensively examine the nonsilica-based infrared fiber. Materials, attenuation, dispersion, fabrication, and potential applications for these new fibers will be explored in depth.

Temperature sensing with infrared fibers is the specific application investigated in this research. Chapter 4 presents a historical, experimental, and somewhat theoretical review of fiber optic temperature sensing methods. Pyrometry, the temperature-sensing technique applied in the experimental part of this report, will be discussed in Chapter 5. Then Chapters 5 and 6 will describe and detail the actual proof-of-concept experiment; that is, an infrared optical fiber pyrometer for high-temperature measurements.

## 2.0 Principles of Silica-Based Optical Fibers

We will begin with a brief review of silica-based optical fibers; that is, their electrical, mechanical, and geometrical properties. Dispersion and loss characteristics for these fibers will be highlighted here, and then compared to the same characteristics for nonsilica-based infrared fibers. Fabrication techniques will be similarly examined.

### 2.1 *Basic Parameters*

The index of refraction,  $n$ , of glass is given by equation (2-1):

$$n = \frac{c}{v} , \quad (2-1)$$

where  $c$  is the speed of light in free space, and  $v$  is the speed of light in the glass. An optical fiber is a glass rod of index  $n_1$  surrounded by a glass tube of index  $n_2$ . The rod is referred to as the core of the fiber and the tube is the cladding.

A ray of light propagating down the core will be totally internally reflected at the core-cladding boundary if Snell's Law, given in equation (2-2), is met.

$$\sin \theta > \frac{n_1}{n_2}, \quad (2-2)$$

where  $\theta$  here is shown in Figure 1 [2]. If equation (2-2) is not met, the rays will leak into the cladding and loss results.

In referring to Figure 2, now call  $\theta$  the launch angle of the light into the fiber.

The numerical aperture ( $NA$ ) of a fiber defines the cone of light accepted into the fiber, in terms of the maximum launch angle. From Figure 2, the  $NA$  is equal to  $\sin \theta_1$ , where  $\theta_1$  is the half-angle of the cone. Thus, from Snell's Law,

$$NA = \sin \theta_1 = n_1 \sin \theta_2. \quad (2-3)$$

This parameter can therefore be expressed solely in terms of the indices of refraction of the core and cladding, as shown in equation (2-4)

$$NA = \sqrt{n_1^2 - n_2^2}. \quad (2-4)$$

The parameter  $\Delta$  is a measure of the difference between the indices of refraction of the core and cladding and is given by equation (2-5) [3].

$$\Delta = \frac{n_1^2 - n_2^2}{2n_1^2} \approx \frac{n_1 - n_2}{n_1}. \quad (2-5)$$

The  $NA$  can then be approximated in terms of  $\Delta$ ;

$$NA \approx n_1 \sqrt{2\Delta}. \quad (2-6)$$

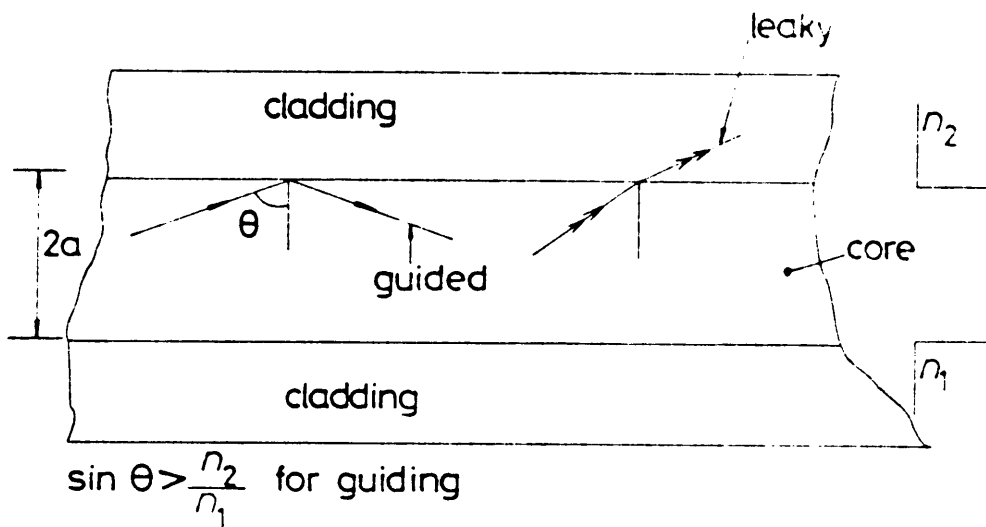


Figure 1. Reflection and Refraction in an Optical Fiber [2]

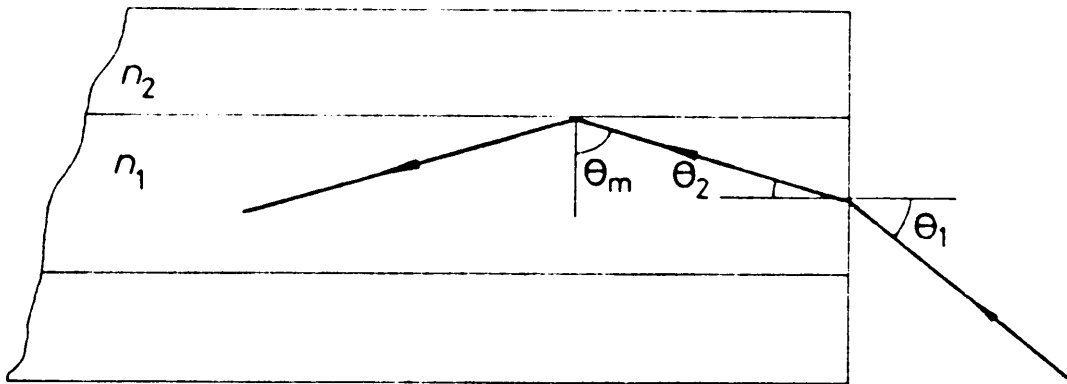


Figure 2. The Numerical Aperture of an Optical Fiber [2]

Typical values for the  $NA$  of a silica fiber range from 0.10 to 0.30.

In order to physically obtain the requirement that  $n_1 > n_2$  for guided ray propagation, the silica ( $SiO_2$ ) in either the core or the cladding, or sometimes both, is doped. Dopants such as  $GeO_2$  or  $P_2O_5$  increase the index and dopants such as  $F$  or  $B_2O_3$  decrease it. Other glasses for optical fibers include the borosilicates, germanosilicates, and soda-lime silicates (the last being a combination of silica, an alkaline oxide, and another oxide) [4].

Operating wavelengths are determined from loss and dispersion characteristics, which will be discussed in sections 2.3 and 2.4. Telecommunications applications use operating wavelengths of 850, 1300, and 1550 nm. Sensor applications use wavelengths down to 633 nm or even shorter.

Single crystals, as well as halide, chalcogenide, and heavy metal oxide glasses are recently under investigation for fiber applications at operating wavelengths much longer than those for the "traditional" silica-based fiber [5]. These cases will be examined in detail in Chapter 3.

## ***2.2 Fiber Classification***

Optical fibers are classified according to the number of modes they support and their refractive index profiles [6].

A mode represents an allowed solution to Maxwell's Equations for a specific waveguide; that is, taking the boundary conditions into account. For a detailed discussion of modes,

mode theory, and optical fiber electromagnetic field theory, see reference [7]. Simply stated, a mode is a possible path for a light ray traveling down the fiber [6].

A single-mode fiber supports one mode that has two mutually orthogonal polarizations. A multi-mode fiber is able to support up to thousands of modes. The total number of modes that one fiber supports depends on the  $V$  number of the fiber, as defined in equation (2-7) below [8].

$$V = \frac{2\pi a}{\lambda} \sqrt{n_1^2 - n_2^2}, \quad (2-7)$$

where  $\frac{2\pi}{\lambda} = k$ , the propagation constant of the mode,  $\lambda$  is the wavelength of operation, and  $a$  is the core radius of the fiber [3, 8].

To achieve single-mode operation, the  $V$  number must fall below a certain cutoff point. Specifically,  $V \leq 2.405$ .

The two categories for classifying an optical fiber on the basis of refractive index profiles are step-index and graded-index. For step-index fiber the core and cladding both have constant indices, and there is a distinct change between these indices at the core-cladding boundary. For graded-index fiber there is a gradual change in the index of the core: it is highest at the center of the core and decreases until it reaches the index of the cladding, which is constant [6].

Different types of fiber have different dimensions and propagation paths. Single-mode fiber generally has a core diameter of 2-10  $\mu\text{m}$ , with an outer diameter of about 125  $\mu\text{m}$ . Light rays basically travel straight down the core. Multi-mode fiber has a core of 50-100  $\mu\text{m}$ , with an outer diameter of 125 or 140  $\mu\text{m}$ . Obviously the larger core allows

more modes to propagate. In step-index fiber, the paths of light are such that there is substantial dispersion (pulse-spreading). Graded-index helps to limit this dispersion since the rays near the center of the core travel slower than the rays near the cladding. (Dispersion will be discussed in more detail in the following section.)

Figure 3 shows a summary of these characteristics.

## ***2.3 Attenuation***

Three major factors contribute to attenuation in optical fibers: absorption, scattering, and radiative (bend) losses.

### **2.3.1 Absorption Loss**

Absorption is defined as the conversion of light power to heat. The mechanisms that cause absorption in optical fibers are due to resonances in the fiber material, that is to say, quantum transitions between different energy levels of the electrons of the fiber material or different vibrational states of its molecules. Electronic transitions usually occur at shorter wavelengths than do vibrational transitions [3].

*Intrinsic* absorption is associated with the basic fiber material, and is the major physical factor that defines a fiber's transparency window over a specified spectral region. As such, it sets the lower limit on absorption for a material. It occurs when the material is in a perfect state with no material inhomogeneities, density variations, or impurities [4].

INDEX  
PROFILE

LONGITUDINAL SECTION

DIMENSIONS

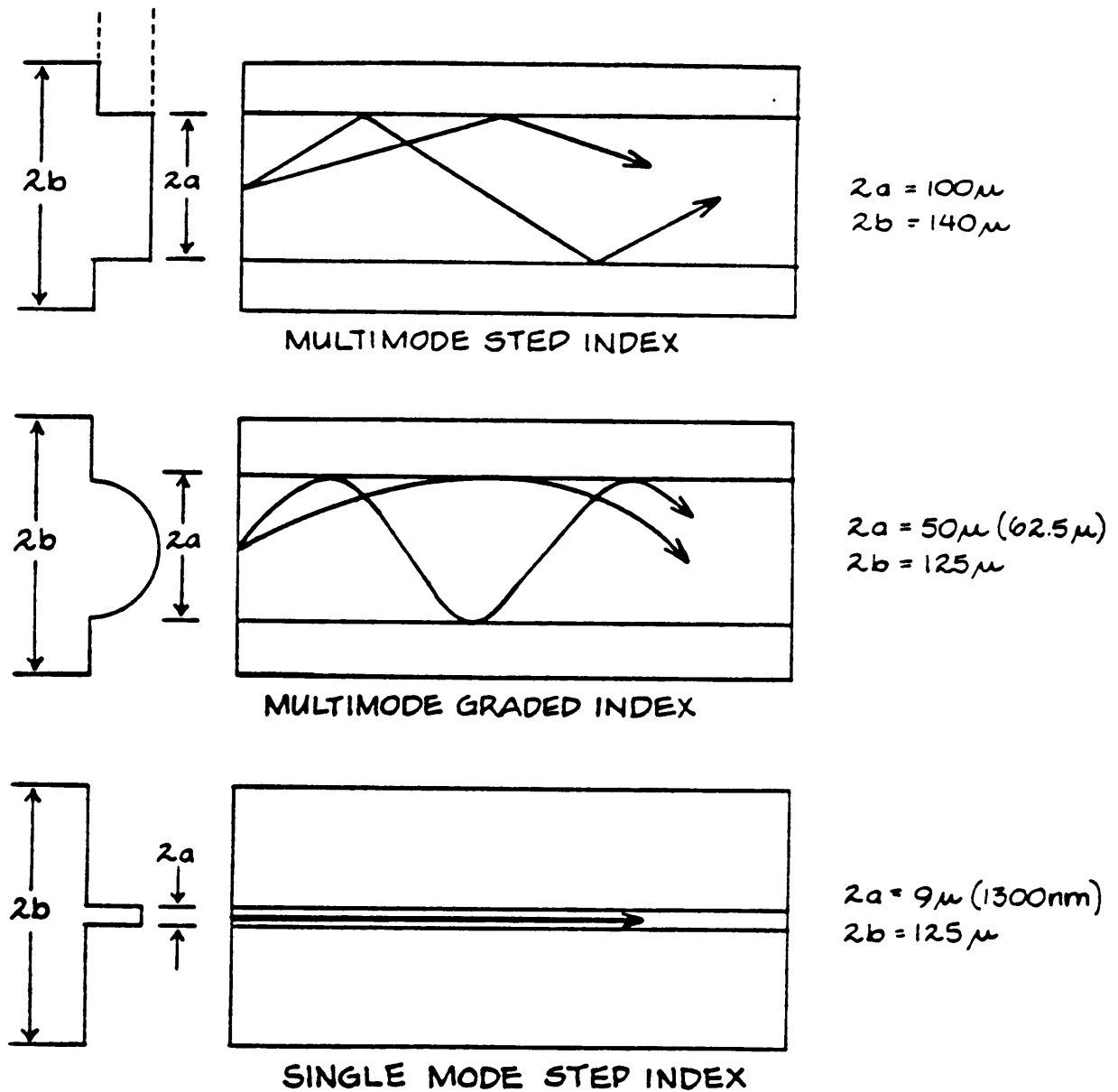


Figure 3. Classification of Optical Fibers

Intrinsic absorption results from electronic absorption bands in the ultraviolet region of the spectrum and from atomic vibration bands in the near-infrared region. Silica fibers are used in a "window" between these two absorption regions [4, 8].

All dielectric materials, hence fibers, have very strong electronic absorption bands in the ultraviolet region. Electronic absorption results when photons have enough energy to excite electrons of the glass materials from a valence band to a conduction band. The energy gap between the valence and conduction bands in pure fused silica is approximately 8.9 eV since the oxygen ions have very tightly bound electrons. Ultraviolet photons at about  $0.14 \mu\text{m}$  are needed to excite these electrons. Thus, the ultraviolet absorption peak occurs at about  $0.14 \mu\text{m}$  for fused silica. The tail decays exponentially and becomes almost negligible in the infrared region of the spectrum [3, 8].

In the near-infrared portion of the spectrum above  $1.2 \mu\text{m}$ , fiber loss is mostly from hydroxyl (*OH*) ions and the inherent infrared absorption of the materials composing the fiber [4]. This absorption tail is caused by molecular vibrations of the chemical bonds between the atoms of the material making up the fiber. An interaction between the vibrating bond and the electromagnetic field of the optical energy results in a transfer of energy from the field to the bond, giving rise to absorption. If only the fundamental vibrations of the silica molecules were important, then the infrared absorption peak would be at  $8 \mu\text{m}$ . However, overtone and combination bands exist at  $3.2 \mu\text{m}$ ,  $3.8 \mu\text{m}$ , and  $4.4 \mu\text{m}$  which also influence the tail. Note that this tail also decays exponentially. Since there are so many bonds in the fiber, this kind of absorption is strong [4, 8].

Figure 4 shows the two absorption tails and how they combine with other forms of loss to form the total attenuation curve for silica fiber.

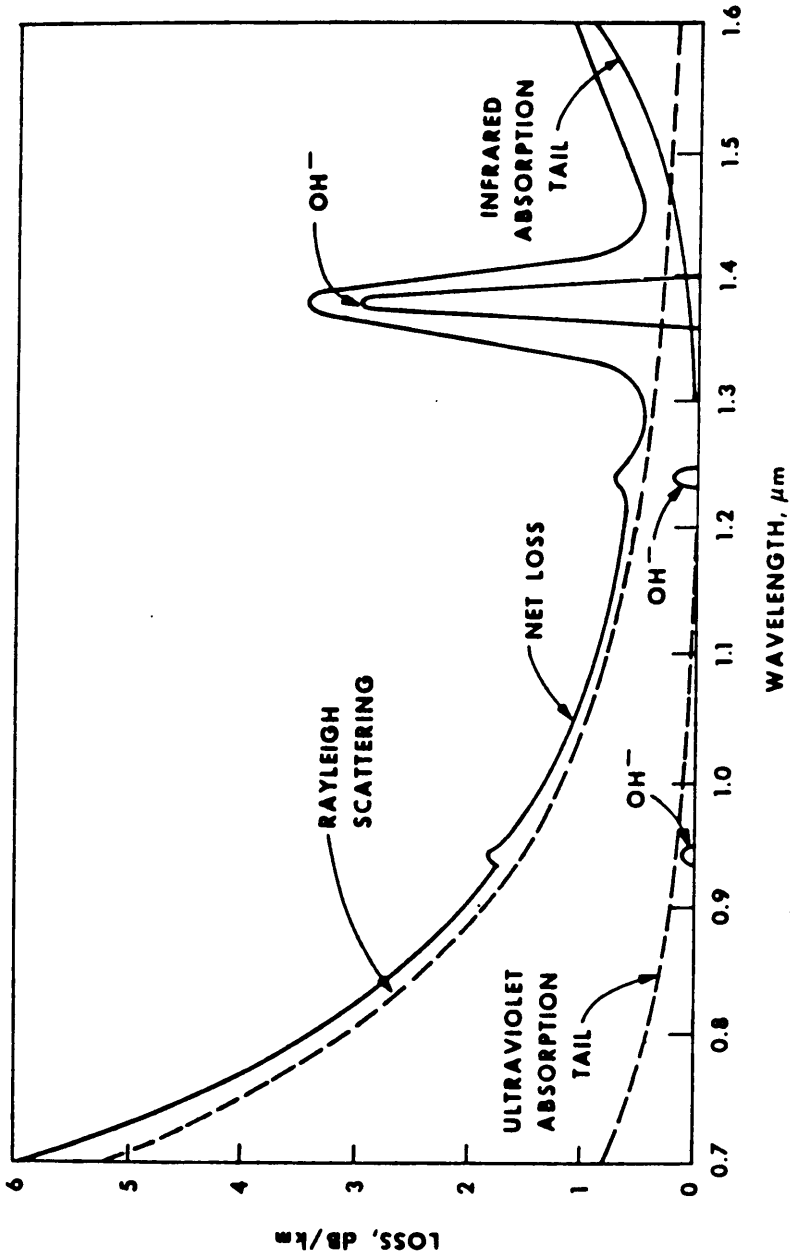


Figure 4. Attenuation Curve for Silica Fiber [8]

*Extrinsic* absorption is the result of impurity atoms in the fiber material. The silica contains dopants and unwanted transition metal (such as iron, chromium, cobalt, copper, nickel, manganese) impurities whose electrons can be excited by lower energy photons than pure fused silica. These materials can shift the ultraviolet absorption tail to longer wavelengths and cause additional absorption bands in the visible and near-infrared regions. The absorption peaks of these transition metal impurities can be broad; hence, several peaks may overlap and broaden the absorption region even more [3, 4, 8].

Impurity absorption is also due to *OH* impurities in the fiber preforms. These ions are mainly the result of the oxyhydrogen flame used for the hydrolysis of the materials used to make the preform. The absorption lines of water are the result of a different mechanism than the absorption lines of the transition metal ions. The *OH* radical of the  $H_2O$  molecule vibrates at a fundamental frequency that corresponds to a wavelength of  $2.8 \mu\text{m}$ . Similar to all other molecular vibrations, the *OH* radical is slightly anharmonic, so that overtones can occur. Therefore, *OH* absorption peaks occur at  $1.39 \mu\text{m}$ ,  $0.95 \mu\text{m}$ , and  $0.725 \mu\text{m}$ , which are the second, third, and fourth harmonics of the fundamental vibrational frequency. It is interesting to note that only one part per million of *OH*<sup>-</sup> in the glass would produce 30 dB/km loss at  $1.39 \mu\text{m}$ . Low levels of attenuation exist between these absorption peaks [3, 4, 8].

Absorption is a very large consideration in the infrared fiber fabrication process. It will be discussed in Chapter 3.

### 2.3.2 Scattering Loss

Most of the scattering loss in fibers is due to Rayleigh scattering. It is caused by the fact that all matter is composed of atoms and molecules that give it a granular appearance on the microscopic scale [3]. For fibers, that translates to very small (compared to the optical wavelength) inhomogeneities in the core material which are a direct result of the fabrication process. Their size is directly related to the temperatures attained during the drawing process. Inhomogeneities include microscopic variations in the material density, compositional fluctuations (especially dopants), or defects [2, 3, 4].

Since Rayleigh scattering varies as  $\lambda^{-4}$ , it decreases dramatically with increasing wavelength. Observed attenuation is close to the Rayleigh limit at about 1  $\mu\text{m}$  and below in "high quality" optical fibers [2]. Please refer again to Figure 4 to notice the  $\lambda^{-4}$  characteristic of Rayleigh scattering. The intersection of the Rayleigh scattering loss curve with the infrared absorption tail usually determines the lower limit of a fiber's loss [8].

Rayleigh scattering is explanatory for particles with dimensions smaller than the wavelength. Larger inhomogeneities, however, such as trapped gas bubbles, also scatter light.

Figure 5 is a pictorial description of the distinction between Rayleigh scattering and intrinsic absorption. In an absorption process, the incident light energy is captured by the impurity atoms, becomes thermal energy, and heats up the core of the fiber. Rayleigh scattering is a spatial redistribution of the light incident on the small discontinuities in the core of the fiber; it is not an absorption of energy. Some of the

light is scattered in the core as both forward and backscatter. And some of it is lost into the cladding [2].

### **2.3.3 Radiative Losses**

Radiative losses are those due to bends. Fibers can be subject to two kinds of bends: bends having radii that are large compared to the fiber diameter, and random microscopic bends of the fiber axis [4].

Consider first large-curvature radiation loss, which, for example, occurs when a fiber cable is bent. Even slight bends force some light, traveling as a guided mode, to be scattered into the cladding and lost. For these types of bends the excess loss is very small and is negligible. As the radius of curvature decreases, the loss increases exponentially until at a certain critical radius this loss becomes observable. If the bend radius is made even smaller than the critical radius, the curvature loss suddenly becomes very large [3, 4].

Microbending loss is expressed as mechanically induced coupling between modes which are guided in the core to modes in the cladding, which are therefore lost from the core [2]. Microbends are repetitive changes in the radius of curvature of the fiber, usually caused by nonuniformities in the sheathing of the fiber or by nonuniform pressures created during cabling [4]. This repetitive curvature causes repetitive coupling of energy between the guided modes and the leaky modes of the fiber [4]. Power coupled to the leaky modes is lost because these modes interact with the lossy fiber jacket and therefore have high absorption losses [3]. Microbends are often purposely induced in fibers to be used as the basis for several types of sensors. Note that microbending losses due to

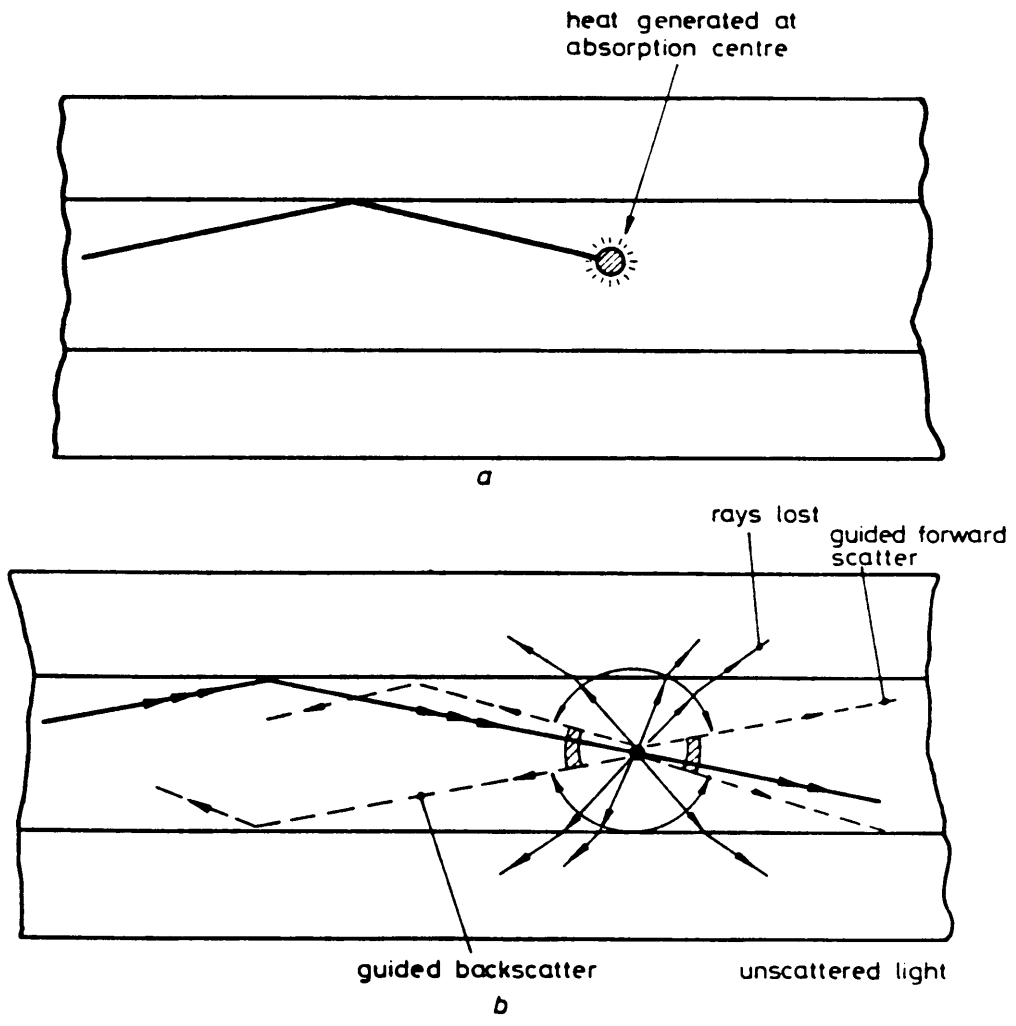


Figure 5. Attenuation due to (a) Absorption (b) Scattering [2]

irregular changes in the fiber axis are more important than radiation losses due to constant curvature.

The peaks and valleys in the total attenuation curve shown in Figure 4 have resulted in the assignment of various "transmission windows" to fibers. Of course, these windows also correspond to wavelengths where economical semiconductor light sources exist (0.8-0.9  $\mu\text{m}$ , 1.3-1.6  $\mu\text{m}$ ).

## ***2.4 Dispersion***

Dispersion, or pulse-spreading, causes an optical signal to be distorted as it travels in a fiber. If observed at an instant in time, pulses increase in length, or if observed at one point, they increase in duration. Since there are different physical reasons for the pulse widths to increase, dispersion has been categorized into three different cases: material dispersion, waveguide dispersion, and intermodal dispersion [3].

Dispersion effects can be explained by examining the group velocities of the guided modes. The group velocity is the speed at which energy in a specific mode travels in a fiber [4].

Dispersion will eventually cause a pulse of light to overlap with its neighboring pulses. When a certain amount of overlap has occurred, adjacent pulses can no longer be individually distinguished at the receiver. As a result, errors at the receiver will occur. Thus, the dispersive properties of the fiber determine its information-carrying capacity [4].

## 2.4.1 Material Dispersion

Material dispersion is caused by the wavelength dependence of the index of refraction of glass. It is the most fundamental type of dispersion. Material dispersion is a subset of *intramodal* dispersion; that is, pulse-spreading that occurs within a single mode. Intramodal dispersion is the result of the group velocity being a function of the wavelength, and is therefore also referred to as *chromatic* dispersion [3, 4]. Hence, material dispersion is due to the wavelength dependence of the refractive index causing a wavelength dependence on the group velocity of any given mode.

Consider the propagation constant of a plane wave in a homogeneous, dispersive medium. The propagation constant of the wave is given in equation (2-8),

$$\beta = nk. \quad (2-8)$$

The group velocity of a wave is defined as follows:

$$v_g = \frac{d\omega}{d\beta}. \quad (2-9)$$

The transit time for a wave traveling a distance  $L$  is

$$\tau = \frac{L}{v_g} = L \frac{d\beta}{d\omega} = L \frac{d\beta}{d\lambda} \frac{d\lambda}{d\omega}. \quad (2-10)$$

Letting  $\lambda = \frac{2\pi c}{\omega}$  and  $c = \frac{\omega}{k}$  gives equation (2-11),

$$\tau = \frac{L}{c} \left( n - \lambda \frac{dn}{d\lambda} \right). \quad (2-11)$$

Equation (2-11) shows that the transit time of the pulses depends on the wavelength if  $\frac{dn}{d\lambda} \neq 0$ . A pulse produced by a source of spectral width  $\Delta\lambda$ , after traveling distance  $L$ , arrives at the receiver spread over a time interval

$$\Delta\tau = \frac{d\tau}{d\lambda} \Delta\lambda. \quad (2-12)$$

The derivative of equation (2-12) describes pulse-spreading;

$$\frac{d\tau}{d\lambda} = -\frac{L}{c} \lambda \frac{d^2n}{d\lambda^2}. \quad (2-13)$$

Note how the second derivative of the index of refraction comes into play here [3].

Figure 6 is a plot of  $\lambda^2 \left( \frac{d^2n}{d\lambda^2} \right)$  vs. wavelength. Note that at around  $1.3 \mu\text{m}$ ,  $\lambda^2 \left( \frac{d^2n}{d\lambda^2} \right) \approx 0$ . This demonstrates that it is theoretically possible to find a source-wavelength region where the pulse-spreading due to material dispersion approaches zero [8]. Here,  $1.3 \mu\text{m}$  is often referred to as the zero-dispersion wavelength.

## 2.4.2 Waveguide Dispersion

If the refractive index of fiber were independent of wavelength, there would still be a small amount of pulse-spreading due to waveguide dispersion [3]. It results because the propagating characteristics of modes are a function of the ratio between the core radius and the wavelength [8].

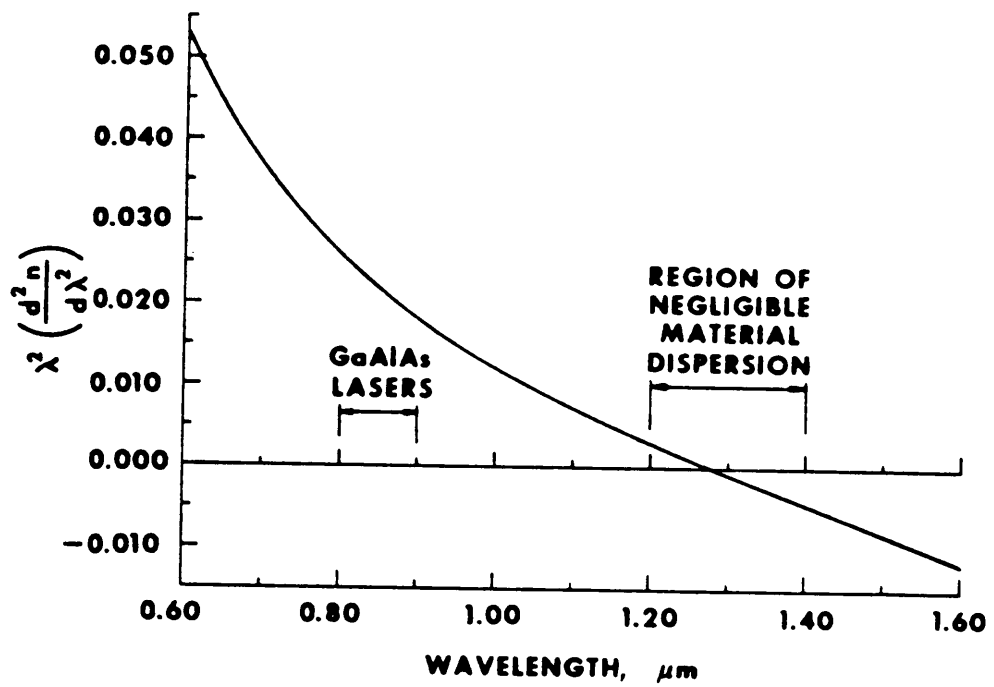


Figure 6. Material Dispersion Curve [8]

First consider the expression for group delay (the time necessary for a mode to travel along a fiber of length  $L$ ) in terms of  $b$ , the normalized propagation constant, as shown below;

$$b = \frac{\frac{\beta^2}{k^2} - n_2^2}{n_1^2 - n_2^2}, \quad (2-14)$$

which, for small  $\Delta$ , can be approximated by

$$b \simeq \frac{\frac{\beta}{k} - n_2}{n_1 - n_2}. \quad (2-15)$$

Hence,

$$\beta \simeq n_2 k (b\Delta + 1). \quad (2-16)$$

Now we determine that the group delay due to waveguide dispersion is

$$t_{wg} = \frac{L}{c} \frac{d\beta}{dk} = \frac{L}{c} \left[ n_2 + n_2 \Delta \frac{d(kb)}{dk} \right], \quad (2-17)$$

which can, for small  $\Delta$ , be approximated by

$$t_{wg} = \frac{L}{c} \left[ n_2 + n_2 \Delta \frac{d(Vb)}{dV} \right]. \quad (2-18)$$

The second term is a function of the fiber core radius and wavelength. Plots of this term are found in the literature [4]. For a fixed  $V$  number the group delay is different for every guided mode.

The modes of a multi-mode fiber reach the far end of the fiber at different times, depending on their group delay. Hence, pulse-spreading results. Note, however, that waveguide dispersion is generally very small when compared to material dispersion in multi-mode fibers, and can usually be neglected [4].

Waveguide dispersion is significant in single-mode fibers. The pulse spread  $\tau_{wg}$  occurring over a distribution  $\sigma_\lambda$  of wavelengths is obtained from the derivative of group delay with respect to wavelength:

$$\tau_{wg} = \sigma_\lambda \frac{dt_{wg}}{d\lambda} = -\frac{V}{\lambda} \sigma_\lambda \frac{dt_{wg}}{dV} = -\frac{n_2 L \Delta \sigma_\lambda}{c \lambda} V \frac{d^2(Vb)}{dV^2}. \quad (2-19)$$

Together, material and waveguide dispersions make up the total chromatic, or intramodal, dispersion of the fiber. It is a function of the spectral width of the source.

### 2.4.3 Intermodal Dispersion

Intermodal dispersion is the result of different values of group delay for each mode at a single frequency. The pulse broadening from this dispersion is the difference in travel time between the highest-order mode and the fundamental mode [4]. This is given by

$$\tau_{mod} = T_{max} - T_{min} = \frac{n_1 \Delta L}{c}. \quad (2-20)$$

Obviously this distortion can be eliminated with single-mode fibers. In step-index fibers,  $\tau_{mod}$  dominates the pulse-spreading by an order of magnitude [4].

## 2.5 Fiber Fabrication Methods

There are two basic methods used for the fabrication of optical fibers: the direct-melt processes and the vapor phase oxidation processes. In the direct-melt method, fibers are drawn directly from the molten state of purified components of glasses. This procedure is generally used for multicomponent glass fibers. In the vapor phase oxidation method, very pure vapors of metal halides react with oxygen to form a white powder of  $SiO_2$  and other dopant particles. These particles are then collected on the surface of a bulk glass and it is all transformed to a homogeneous glass mass by heating without melting (i.e., sintered), to form a preform [4]. The actual fiber is drawn from the preform. During the draw process it is coated; usually with some sort of plastic, for strength and protection.

### 2.5.1 Direct Melt Methods

In the *double crucible* method, glass rods for the core and cladding materials are first made individually by melting mixtures of purified powders to make the appropriate glass composition. Then these rods are used as feed stock for two concentric crucibles; an inner crucible which contains the molten core glass and an outer crucible that holds the molten cladding glass. Fiber is drawn directly and continuously through orifices in the bottoms of the crucibles [4]. The double crucible apparatus is shown in Figure 7 (a).

The strengths of this method include compositional and geometrical flexibility (very high  $NAs$  and large-core fibers, for example), and the potential for continuous operation with a minimum number of steps in the procedure [8]. However, the glass may become

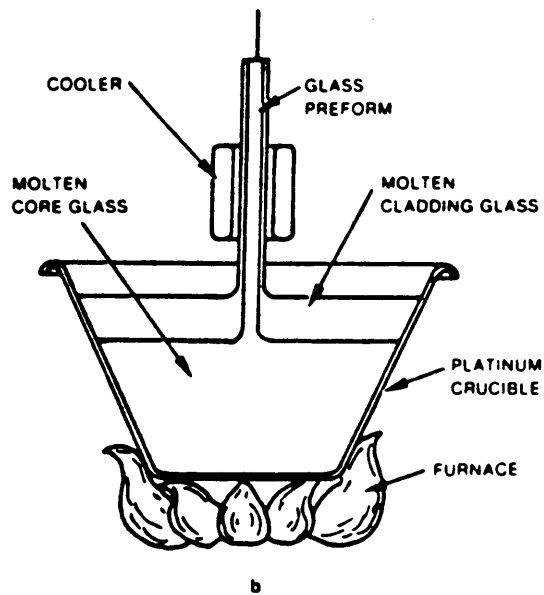
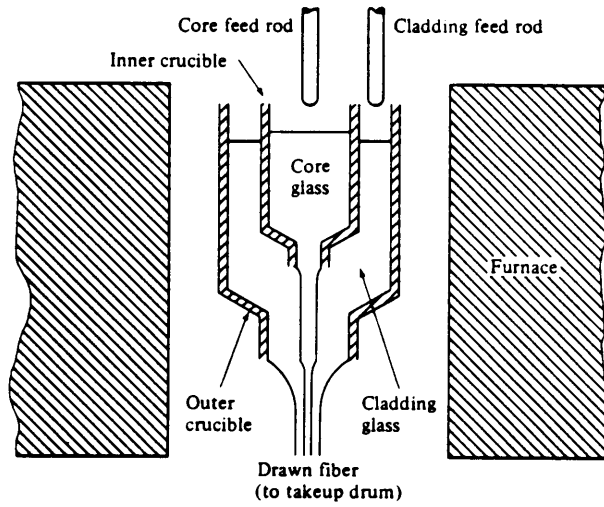


Figure 7. Apparatus for Direct-Melt Methods: (a) Double Crucible [4] (b) Stratified Melt [6]

contaminated during the melting process; usually from furnace and/or crucible impurities.

Figure 7 (b) depicts the apparatus used in the *stratified – melt* method. Molten core material floats on molten cladding material in a single crucible. Both materials are drawn upward through a cooler to make a preform or a fiber. This method has several advantages over others: it offers better control over dirt, contamination, and improper fusion that cause loss at the core-cladding boundary. Note that this technique does not produce low loss fibers, but it does produce high- $NA$ , step-index fibers [6].

## 2.5.2 Vapor Phase Oxidation Methods

The *modified chemical vapor deposition* (MCVD) method of fabricating preforms was invented at AT&T Bell Laboratories in 1974. Figure 8 (a) illustrates this process. It involves externally heating a rotating silica tube (by moving a torch down the length of the tube) to thermally trigger oxidation of chloride precursors that are flowing inside the tube. In the "hot zone," both homogeneous (gas-phase) and heterogeneous (different phases, gaseous precursors, and solid-tube wall) reactions occur. The oxidation reaction produces soot, i.e., finely divided particulate glass material. As this soot flows down the tube, some of it is attracted to the cold walls where it is deposited as a thin, porous layer. The remaining soot flows out the far end of the tube. As the torch moves down the tube and passes the deposited soot, it "zone-sinters" it to a clear glass layer. When the torch reaches the far end of the tube it is returned to the front end and the procedure starts again. The final step in this process is to collapse the tube into a preform. This is achieved by decreasing the torch velocity and allowing the tube temperature to increase.

As heat softens the tube, surface tension shrinks it. The fiber from the preform will have a core consisting of the deposited material and a cladding consisting of the silica tube [8].

Regarding mass production, machines can be easily switched from one fiber design to another, providing a flexibility to meet fiber demand changes. MCVD has been proven to be a process that can produce the highest quality fiber under factory conditions [9].

Next, a scheme of *plasma activated chemical vapor deposition* (PCVD) is illustrated in Figure 8 (b). The main components of the system are the gas supply system, the reactor, and the exhaust pumping system [10].

In the gas supply, the starting materials are metered and mixed in the gaseous phase. The resulting gases (usually mixtures of  $SiCl_4$ ,  $O_2$  with varying contents of say  $C_2F_6$ , and/or  $GeCl_4$ ) are then fed into a silica tube. In a moving nonisothermal plasma which travels along the tube, molecular reactions are stimulated and deposition of the desired glass components on the inner wall of the tube occurs. A compact glass layer can be deposited with each pass of the plasma zone [10]. To make a graded-index preform, approximately 2000 glass layers are deposited this way. No soot is formed by this heterogeneous reaction of metal halides. Quick traverse of the plasma can be used to make very thin glass layers, which result in a very well controlled index profile [8]. Usually the plasma is generated in a microwave cavity [10].

The *outside vapor phase oxidation* (OVPO) or *outside vapor deposition* (OVD) process is shown in Figure 8 (c). A layer of soot is deposited from a burner onto a bait rod (a rotating graphite or ceramic mandrel). The soot adheres to the rod, and, one layer at a time, a porous preform is built up. By properly controlling the constituents of the vapor stream during the deposition process, the glass composition and dimensions desired for

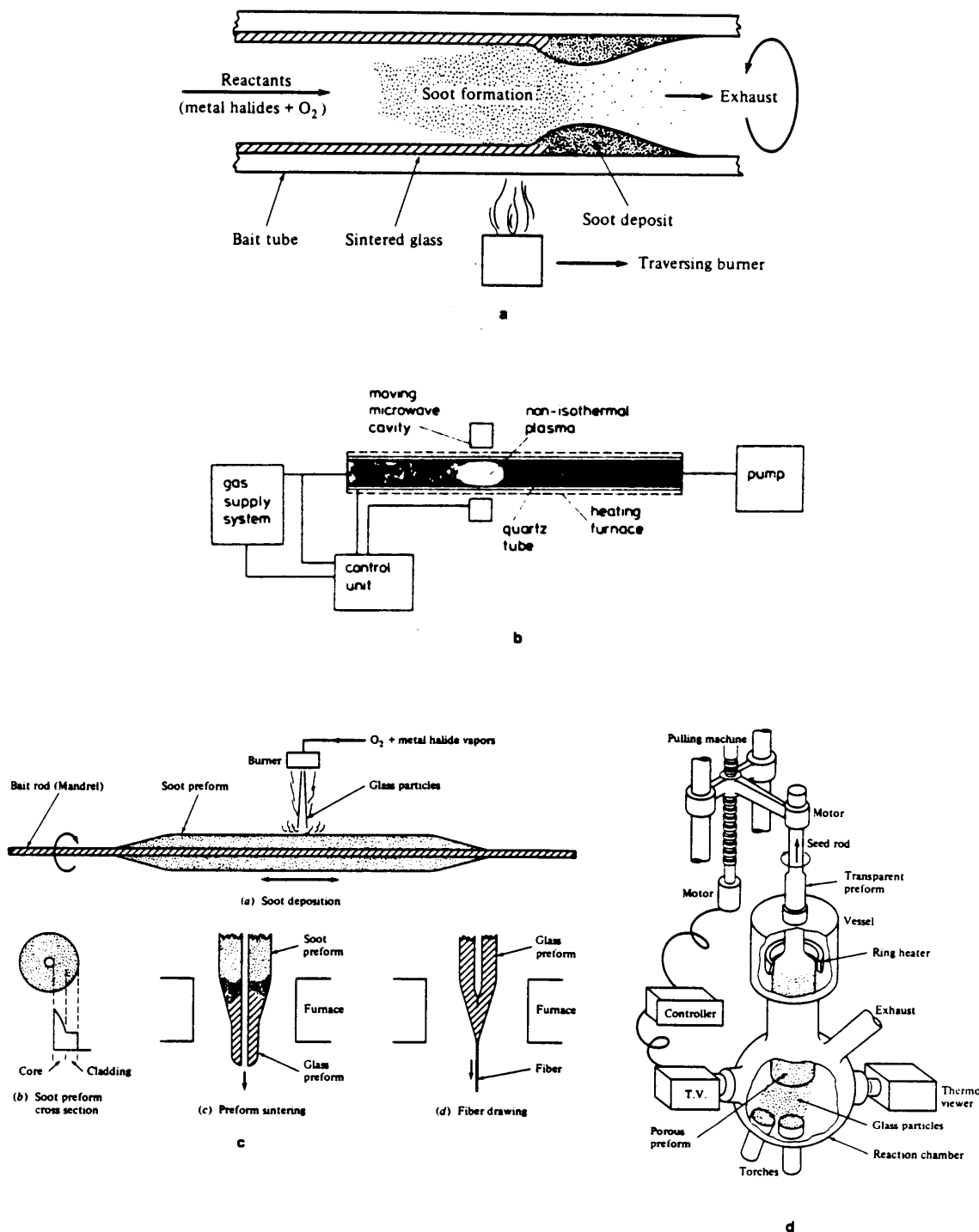


Figure 8. Apparatus for Vapor Phase Oxidation Methods: (a) MCVD [4] (b) PCVD [10] (c) OVPO/OVD [4] (d) VAD [4]

the core and cladding can be incorporated into the preform. Hence, step or graded-index preforms can be produced. When the deposition process is completed, the bait rod is removed and the porous tube is then zone-sintered to make a preform. The central hole in the preform collapses when it is drawn into fiber [4, 8].

Finally, Figure 8 (d) is a schematic of the *vapor phase axial deposition* (VAD) method. The silica particles are formed in the same manner as with the OVPO/OVD method. As the particles emerge from the torches, they are deposited on the end of a silica glass seed rod. By moving the rod upward, a porous preform is grown in the axial direction. Note that the rod is continuously rotated to establish a cylindrical symmetry of the particle deposition. As the porous preform moves upward, it is heated in a narrow, localized zone and is transformed into a solid, transparent rod preform. This then, is the preform that is subsequently drawn into fiber [4].

There are three advantages to the VAD preform fabrication technique: the preform does not have a central hole; the preform can be fabricated in continuous lengths which can affect product yields and production costs; and a clean environment is achieved since major components of the system are tightly connected to each other (i.e., the deposition chamber and the ring heater) [4].

The MCVD, PCVD, OVPO/OVD, and VAD techniques have three key features common to each of them. First, the desired glass constituents are available in the form of volatile gaseous compounds of high purity. Second, these compounds can be mixed almost ideally in the gas phase. Lastly, reactions, deposition, and purification occur directly in the gas phase at the gas/solid interface or on soot particles smaller than 10 Å.

## 3.0 Nonsilica-Based Infrared Fibers

Historically, nonsilica-based infrared fibers were made in the 1960's for imaging bundles and remote sensors, but they had losses of 20,000 dB/km. Infrared fiber technology essentially stood still during the rapid advancements in silica fibers in the 1970's. As a result of this progress, it was clearly understood (as discussed in Chapter 2) that the intrinsic optical attenuation in silica-based fiber originates from Rayleigh scattering, the ultraviolet absorption tail, and the infrared absorption edge. Actual attenuation measurements of 0.2 dB/km correspond closely to the ultimate theoretical loss for a silica fiber. As part of a drive to achieve lower overall losses, there is now a trend in research to investigate nonsilica glasses. In order to fabricate fibers with "ultralow" loss, it is necessary to develop new infrared fiber materials that have smaller Rayleigh scattering loss than silica fibers, and which have the infrared absorption edge at longer wavelengths [5]. Recall that the silica-based material transmission is limited in the infrared at 3.0  $\mu\text{m}$  by the multiphonon absorption tail, and at 2.8  $\mu\text{m}$  by *OH* perturbations [11].

Potential materials for ultralow loss infrared fibers are categorized into four groups: halide glasses, heavy metal oxide glasses, chalcogenide glasses, and crystalline materials. These materials can be further classified for use in either the near, mid, or far infrared.

### ***3.1 Fibers for the Near Infrared***

The near infrared is the 0.75-2.5  $\mu\text{m}$  range. Fibers used in this range are the silica-based fibers discussed in Chapter 2.

Pure silica core fiber and high  $NA$  fiber of more complicated silicate composition are likely to find applications as short distance links, where ultralow attenuation is not the major concern. Thus, pure silica, borosilicate and germania, and/or phosphorous doped silica fibers are most likely to be the major materials used in the near infrared for both long haul and short haul applications [12].

The most common telecommunications fiber is the germania doped silica core fiber. It has been manufactured with very low intrinsic loss and has good transmittance at 0.85, 1.3, and 1.55  $\mu\text{m}$ .

Note that fibers up to 10 km long cannot contain any flaws that could result in failure under normal operating conditions. In general, fibers must retain high breaking strain ( $> 1$  percent) over long lengths for up to 20 years in their working environment. The total flaw population is the sum of the intrinsic and extrinsic flaws. Extrinsic flaws created during manufacture need to be eliminated or reduced to specified low levels to maximize fiber strength.

## 3.2 *Fibers for the Mid Infrared*

The mid infrared is the 3-5  $\mu\text{m}$  range. Fibers used in this range are made of halide or heavy metal oxide glasses.

### 3.2.1 Halides

Halides have been considered to have the most appropriate optical properties for ultralow loss fibers because their bandgap is large and their multiphonon absorption edge is found in a longer wavelength region than silica. Beryllium fluoride based (fluoroberyllate) glasses were investigated as early as 1949 and were found to have very low indices of refraction (1.2747) and optical dispersion. However, little emphasis was placed on them because of the general toxicity of beryllium compounds and the hygroscopic (readily absorbing moisture) nature of these particular glasses. Then the discovery of fluorozirconate ( $ZrF_4$ ) glasses by Poulain, et al, [13] in 1975 and fluorohafnate ( $HfF_4$ ) glasses a few years later generated a great deal of interest in fluoride-based glasses as mid infrared fiber optic materials. Since then, the major thrust in infrared glass material research has been on fluoride based glasses. Therefore, most of this section will be devoted to fluoride based infrared fibers. They contain about 50-60 mole percent  $ZrF_4$  or  $HfF_4$  together with 30-40 mole percent  $BaF_2$  and a number of alkali, alkaline earth, transition, and rare-earth fluorides (such as  $GdF_3$ ,  $AlF_3$ ,  $LaF_3$ ,  $PbF_2$ ) primarily to improve glass stability [5, 12]. These glasses have potential ultralow loss transmission capability in the 2-4  $\mu\text{m}$  region. Possible uses include those in medicine, the transfer of radiation in infrared optical systems (sensors,

for example), and in repeaterless, long haul communications links. Fluoride based fibers are transparent from 0.23-7  $\mu\text{m}$ , but they will be used from 2-4  $\mu\text{m}$ .

The minimum loss for  $ZrF_4$ ,  $HfF_4$ , and  $AlF_3$  based glasses was predicted as  $10^{-2}$  to  $10^{-3}$  dB/km in the 2-5  $\mu\text{m}$  region. The zero material dispersion point occurs at about 1.6-1.7  $\mu\text{m}$  for the  $ZrF_4$  and  $HfF_4$  based glasses, and at 1.48  $\mu\text{m}$  for  $AlF_3$  based glasses. The impurity absorption losses in  $ZrF_4$  based glasses were determined quantitatively and shown that the absorption intensities for transition metal ions and rare-earths would be relatively weak in the 2-5  $\mu\text{m}$  region [5].

In 1982, researchers reported another family of fluoride glasses based on  $ThF_4$  and trivalent ( $Yb$ ,  $Y$ ,  $Tm$ ) fluorides and/or divalent ( $Zn$ ,  $Mg$ ) fluorides with  $BaF_2$ . The infrared transmission for these glasses goes out to 7-8  $\mu\text{m}$ . More recently, (1987) Lucas, et al, [14] have been experimenting with a new family of indium based fluoride glasses. Transmission for these halide glasses also goes 1  $\mu\text{m}$  further out into the infrared.

The  $ZrF_4$  based glasses are low melting materials. The crystallization temperature is 370-450  $^{\circ}\text{C}$ ; the fusion temperature is 550-600  $^{\circ}\text{C}$ ; and the glass transition temperature is around 330  $^{\circ}\text{C}$ . They have high thermal expansion coefficients. The index of refraction is about 1.52, and does not change very much with variations in the base composition. Hence, some dopants are needed in the base glass in order to control the refractive index.

Regarding loss, it seems that the intrinsic loss in  $ZrF_4$  based fluoride fibers should be around 0.01 dB/km at 2.5  $\mu\text{m}$ . However, the experimental loss still (1987) remains more than an order of magnitude higher than the estimated value [15].

At the present development stage, a major problem with all of these materials is the proximity of the glass transition temperatures to the crystallization temperatures. This results in devitrification problems and sometimes the presence of 10-50  $\mu\text{m}$  microcrystallites. The growth of these crystals in the glass depends on the glass's viscosity. The fluoride glasses have a narrow working range and the viscosity is strongly dependent on temperature. Therefore, emphasis is placed on glass compositions with three or more components to enhance glass stability and adjust the viscosity to values appropriate for preform fabrication and fiber drawing [12, 16].

### 3.2.2 Heavy Metal Oxides

Basically, only  $\text{GeO}_2$  based glasses have received great attention for the fabrication of infrared fibers, although other glasses in this category include  $\text{La}_2\text{O}_3$ ,  $\text{TeO}_2$ , and  $\text{CaO} - \text{Al}_2\text{O}_3$  [5, 11]. From the theoretical point of view,  $\text{GeO}_2$  fibers are the least attractive among the candidates as infrared fibers because the transmitting wavelength window in the infrared region does not extend as far as other candidates [17].

To date, however,  $\text{GeO}_2$  based fiber is the most promising candidate for achievement of losses less than 0.2 dB/km, the loss limit of silica fiber, because it is prepared by a VAD method with a dehydration process. This technique has a higher degree of purity than any of the other fabrication methods for infrared fibers. No absorption can be found near 3  $\mu\text{m}$  due to  $\text{OH}$  for the glass prepared by the VAD method. A large amount of  $\text{OH}$  is usually found in glass formed by the crucible technique. It is unlikely that  $\text{GeO}_2$  fibers will ever surpass  $\text{SiO}_2$  fibers in their performance [17].

### ***3.3 Fibers for the Far Infrared***

The far infrared range is 8-12  $\mu\text{m}$ . Fibers used in this range are made of chalcogenide glasses or crystalline materials.

#### **3.3.1 Chalcogenides**

These glasses are so named because they contain one or more of the chalcogenide elements *S, Se, T* together with one or more of the elements *Ge, Si, As, Sb* and a number of others [12]. They have a stable vitreous state with an extensive glass forming region. They have one advantage in that their stability against crystallization makes fabrication of long, homogeneous fiber possible. Crystallization rates are generally slow [18]. They find applications in thermal imaging, sensing and tracking, remote spectroscopy, and delivery of both *CO* and *CO<sub>2</sub>* laser radiation.

Although bulk chalcogenide glasses have been researched for many years, the development of low loss fibers is still in an early stage. Throughout much of their transmission waveband, attenuation is dominated by extrinsic processes, of which absorption due to impurities is the most serious. Losses on the order of 0.1 dB/m have been achieved in several wavebands, but these are narrowly defined by impurity absorptions. It is interesting to note that one such loss minimum coincides with the output waveband of the *CO* laser, thus enabling tens of watts of power to be delivered over a few meters. However, there is a need to extend the transmission window to longer

wavelengths and to reduce losses at 10.6  $\mu\text{m}$  below 1 dB/m so that significant amounts of  $\text{CO}_2$  laser power can be transmitted [19].

In chalcogenide glasses the band-gap energy decreases with decreasing bond strength. Therefore, the absorption edge occurs at the shortest wavelengths in glasses based on sulphides and at the longest wavelengths in glasses based on tellurides.

Intrinsic losses have been estimated to be less than 0.1 dB/km in the 5-6  $\mu\text{m}$  band, but it is clear that more detailed studies of loss mechanisms will be necessary if the realistic potential losses of chalcogenide fibers are to be accurately established, and ultimately to be attained. Presently, the role of impurities is only understood qualitatively. Effects of impurities, defect centers, and glass composition on the weak absorption tail need to be examined further.

The improvements in purification and processing techniques that will be needed in order to reduce losses to intrinsic levels may be impossible. Clearly, the potential losses of chalcogenide fibers have not been fully established yet.

Estimates of the levels to which extrinsic scattering might be reduced suffer from a lack of direct measurements and from the difficulty of examining chalcogenide fibers using standard optical microscope techniques.

### **3.3.2 Crystalline Materials**

Typical crystalline materials have been classified into two areas: polycrystal and single crystal. Polycrystalline materials are extruded and single crystals are grown.

Halide crystals are a logical choice for infrared fibers since their fundamental phonon absorption bands are located in the far infrared. The optical transparency of these materials covers a much broader spectral range than those of other infrared materials. Theoretical calculations show the superiority of halide crystals as fiber materials with losses as low as  $10^{-3}$  dB/km [5].

*TlBrI* (KRS-5) has been researched extensively. It is superior in mechanical and chemical properties to other crystals for infrared fiber. It has a relatively low melting point and is transparent from 0.63-35  $\mu\text{m}$ . The minimum loss stated above occurs at 7.0  $\mu\text{m}$ . The total attenuation coefficient varies as  $\lambda^{-2}$  as opposed to the  $\lambda^{-4}$  dependence in silica fiber. The  $\lambda^{-2}$  dependence results from the combination of bulk scattering from large scale optical imperfections and surface scattering and absorption [5]. Its transparency gradually decreases in shorter wavelengths. At 10.6  $\mu\text{m}$  the refractive index is 2.37.

KRS-5 has been successfully extruded, as has *AgBr*. The mechanical properties of thallium and silver halides are best suited to extrusion, so most of the work on polycrystalline fibers has been concerned with these materials.

Single crystal fibers offer alternatives to polycrystalline fibers because they do not have scattering centers associated with grain boundaries in polycrystalline fibers.

## 3.4 Fabrication Methods

### 3.4.1 Fluoride Glass Fibers

One synthesis method for fluoride glass compounds is a preform method, which consists of (1) purification of raw materials, (2) melting of mixtures into solid-phase raw materials, (3) casting glass melts into fiber preforms, and (4) drawing preforms into fibers [15]. This section considers step 3 of this process. Another method is the crucible technique, which is a modified version of the technique presented in Chapter 2. Each of these two processes have their own advantages and disadvantages. The preform method is carried out at relatively low temperatures and materials are thermally reworked at low viscosity and at a temperature far from the crystallization temperature, but it is difficult to form a smooth interface between the core and cladding. In the crucible method, fabrication is performed at a very high temperature and the material tends to crystallize during the drawing process. If the viscosity is sufficiently increased at the drawing temperature, a core-cladding structure will be formed easily with this technique [5]. Chemical vapor deposition methods are not used for the synthesis of fluoride glass except for glasses like  $BaF_2$  that have just one component [15].

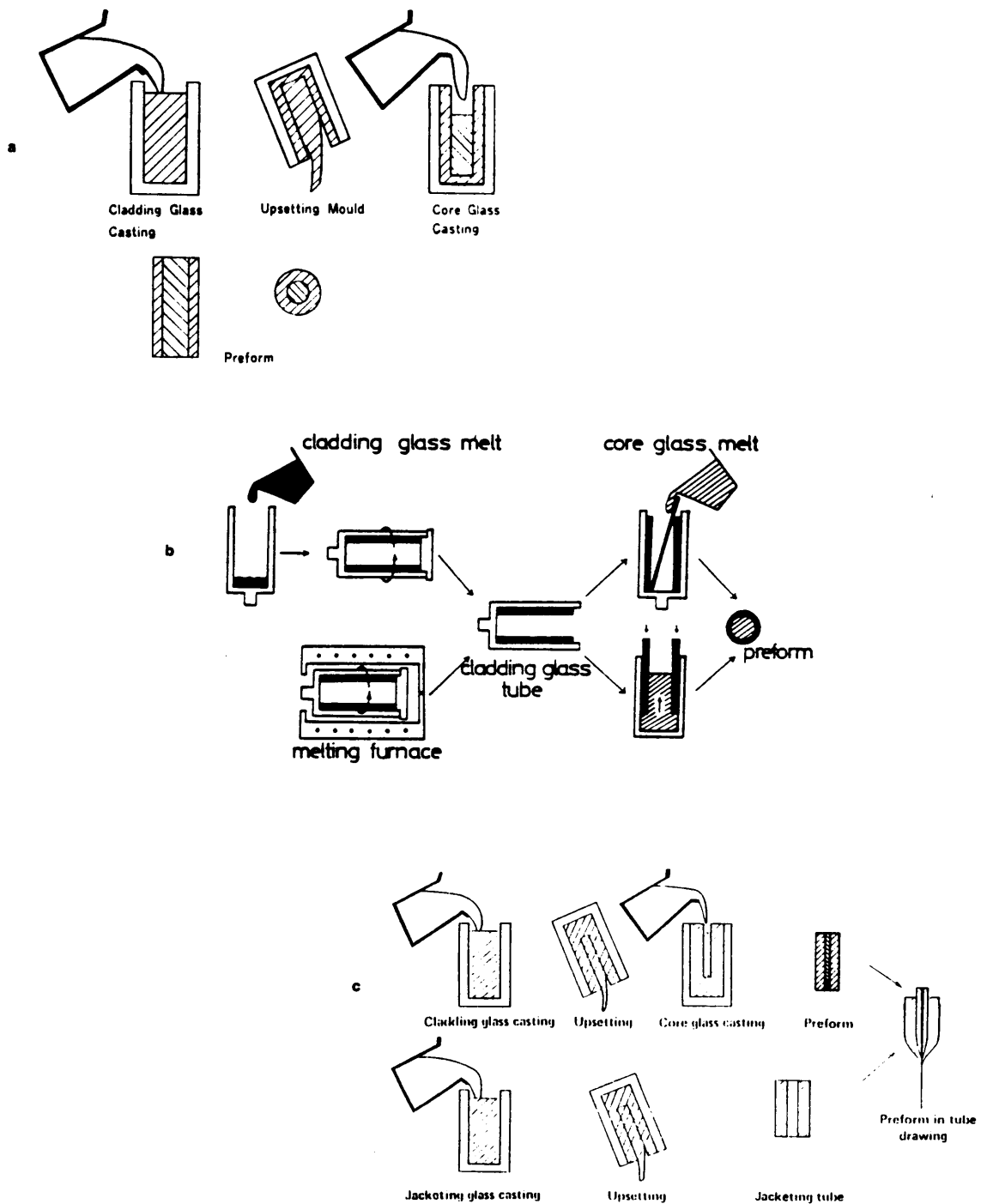
There are several ways in which to cast a fiber preform. These include built-in casting, rotational casting, and suction casting.

Figure 9 (a) shows the *built-in* casting process. The cladding glass melt is poured into a cylindrical mold which is preheated to approximately the glass transition temperature. This is immediately turned over so that the melt in the middle part of the mold runs out.

Then the core glass melt is poured into the central cylindrical tube and annealed. Typical preforms resulting from this procedure have a 10 mm outer diameter and are 120 mm long. These preforms are often jacketed with a Teflon-FEP tube (which has a refractive index of 1.338). 110 m of fiber can be drawn from a 100 mm preform [20]. Designed core diameters, ranging from 20-80  $\mu\text{m}$ , and outer diameters ranging from 100-300  $\mu\text{m}$  can easily be achieved. Fiber lengths reach up to 500 m [5].

The *rotational* casting process is depicted in Figure 9 (b). The cladding glass melt is poured into a cylindrical mold, once again preheated to the glass transition temperature. It is then rotated at speeds greater than or equal to 3000 rev/min. This permits the attainment of a highly concentric fluoride cladding glass tube whose inner diameter is precisely controlled by the initial volume of injected glass. The fluoride glass tubing could also be prepared by melting directly in the rotating mold, following that with a rapid quench to the glass transition temperature, and a final annealing step. Then the core glass is transferred to the tube by either pouring the melt down a fluoride bait rod or by dipping the tube into the core melt (to avoid bubble formation). Long-length fibers with core diameters between 70-150  $\mu\text{m}$  and cladding thicknesses from 10-30  $\mu\text{m}$  can be drawn from the resulting preform [21].

Built-in and rotational casting methods cannot be applied to single-mode fiber fabrication because it is difficult to obtain fiber with a core diameter small enough for single-mode regime. The procedure to prepare single-mode fiber is shown in Figure 9 (c). They are made with a preform and jacketing tube. The preforms are obtained from a built-in casting method, which can provide preforms with a cladding/core ratio greater than 5. (This is necessary in order to eliminate the effect of *OH* ion and structure fluctuation at the boundary between the preform and jacketing tube on transmission



**Figure 9. Fluoride Fiber Fabrication Techniques:** (a) Built-In Casting [5] (b) Rotational Casting [21] (c) Single-Mode [22]

loss.) The jacketing tubes are obtained from a "mold upsetting" method which is similar to built-in casting. The refractive index of the jacketing tubes is higher than that of the cladding. After forcing the central part of the mold of the casted glass flow out, the U-shaped mold is annealed and cooled to room temperature. The tubes are made by boring. The preform is then placed in the jacketing tube and both of these are inserted into a Teflon-FEP tube and drawn into fiber [22].

A more recent (1987) procedure for fabricating single-mode fibers is the *suction* casting technique. In suction casting, a specially designed cylindrical mold with a reservoir at the bottom is used. First the cladding melt is poured into the mold. Before it is completely solidified, the core melt is poured on the cladding melt. The volume shrinks during cooling. As the cladding glass shrinks, it derives suction flow for the core glass along the mold axis. A uniform core/cladding ratio is thus obtained. This ratio can be changed by changing the reservoir volume [15].

The *crucible* technique shown in Figure 10 (a) uses a single crucible apparatus. The coating applicator applies a plastic clad to the fiber. Note that the temperature range for fiber fabrication is limited because the working range for fluoride glasses is generally much narrower than that for silicate glasses. There is also a high crystallization rate around 300-400 °C. For this reason fibers must be drawn with the application of a modified single crucible design [5].

Researchers have, however, drawn fiber using a two crucible draw set-up. This is shown in Figure 10 (b). Molten fluoride glasses are drained from an upper melting crucible to a lower single draw crucible maintained at the glass softening temperature range [5].

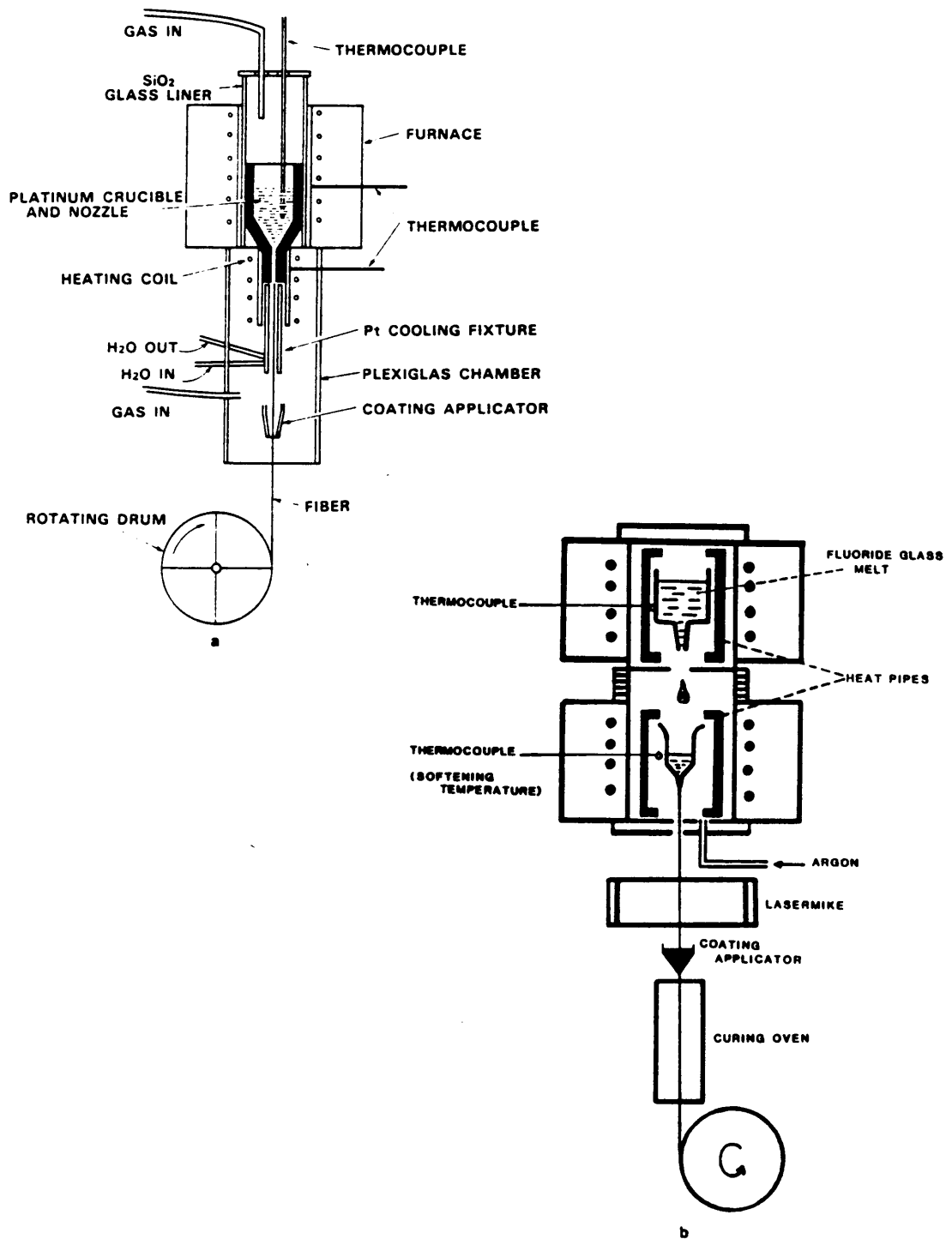


Figure 10. Fluoride Fiber Fabrication Techniques: (a) Single Crucible [5] (b) Double Crucible [23]

Note that in fluoride fiber drawing, an FEP tube is often used for preform jacketing. It is used to suppress surface crystallization induced by water in the atmosphere. An FEP coated fiber is obtained when the jacketed preform is drawn. This coating brings some disadvantages in both mechanical and optical performances for a glass-cladded fiber. The disadvantages are due to its low refractive index and nonchemical activity. Therefore, it is necessary to develop drawing and coating techniques similar to those established in silica fiber fabrication [15].

### 3.4.2 Heavy Metal Oxide Fibers

$GeO_2$  glass fiber has been fabricated by the VAD method. But since  $GeO_2$  glass differs from silica glass in both physical and chemical characteristics, (the dehydration temperature, for example) the process must be somewhat modified [17].

$GeCl_4$  is used as the main raw material and  $SbCl_5$  is used as the dopant raw material. They are bubbled with  $Ar$  gas and transferred into an oxyhydrogen flame where they are hydrolized into oxide particulates which are in turn deposited on the end of a starting substrate. This substrate is then spun and vertically lifted. A porous preform is sintered to the transparent preform by an electric furnace that is charged with helium. The sintered preforms are usually 15 mm in diameter and 100 mm long [5].

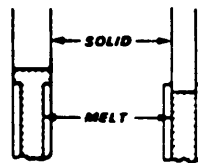
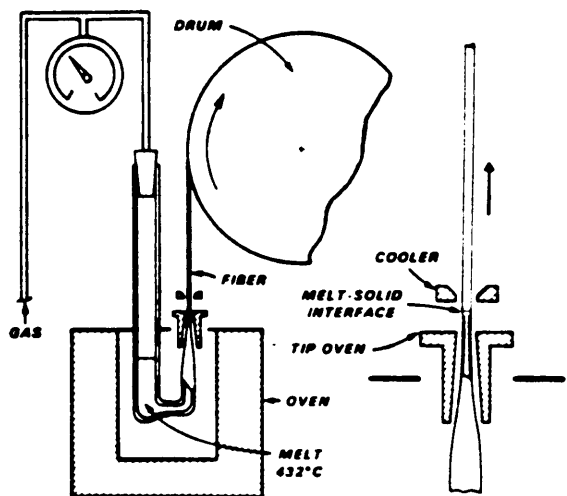
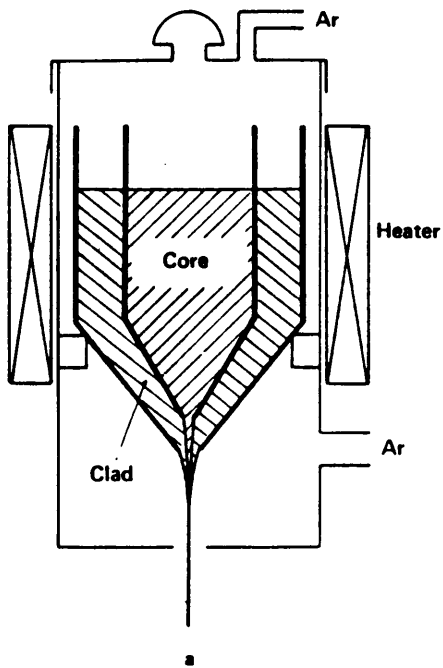
Crucible techniques can also be used to make various heavy metal oxide glass fibers. Tellurium oxide based fibers have been fabricated with gold crucibles [5].

### 3.4.3 Chalcogenide Fibers

Generally, bulk materials must be synthesized before fibers can be drawn. Arsenic-sulfide glasses are formed into glass rods 8-15 mm in diameter and 80-120 mm long. These rods are zonally heated and drawn into fibers. There are severe problems encountered in the fabrication of cladding glass tubes and core glass rods with optical polished surfaces. Therefore, the preform method is usually limited to the fabrication of unclad fiber [5].

A specially designed concentric crucible for drawing arsenic-sulfur glasses has been developed. Investigators have prepared chalcogenide fiber using a Pyrex glass double crucible assembly as shown in Figure 11 (a). Its design is very similar to the conventional double crucible used to make silicate fibers, except that it has a long nozzle pipe which is useful for cooling the glass as it exits through the nozzle. This is necessary because of the narrow working range of this glass [5].

The crucible has a core glass in the inner section and a cladding glass in the outer section, and is then fitted into an electric furnace. The inside of the furnace is maintained under an inert atmosphere to prevent the formation of arsenic and sulfur oxides. Then the temperature of the assembly is increased to about 400 °C, and the core and cladding glasses descend from the nozzle and form a small drawing cone beneath it. If a stable symmetrical cone of flowing glass exists beneath the nozzle, then the drawing is satisfactory. The core/cladding diameter ratio can be varied by changing the nozzle diameter ratio between the two crucibles. Fiber diameter ranges from 100-300  $\mu\text{m}$ , and fibers longer than 1 km are easily fabricated [5].



b

Figure 11. Fabrication Methods for Chalcogenides and Crystalline Fibers: (a) Double Crucible for Chalcogenide Glass [24] (b) Fiber Crystal-Growing Apparatus [25]

So far, however, a low-loss clad fiber has not been fabricated by these methods [26].

### 3.4.4 Crystalline Fibers

Two methods have been used to form crystalline fibers. The first approach involves solid-state recrystallization by extrusion from the original crystal rod. The second technique is that of growth from the melt phase.

Polycrystalline fibers without cladding have been made extensively from *KRS-5*, *KRS-6*, and *TlBr* by the *extrusion* method. Using this method, long polycrystalline fibers can be prepared at relatively high speed, although the resulting fiber is usually quite fragile. As an example, consider the fabrication of *KRS-5*.

The starting material is melted in a nitrogen atmosphere, and is cast and sealed into glass ampoules. It is then crystallized. The crystal ingot is shaped by mechanical machining to 10 mm in diameter and 30-40 mm long. This is the preform, which is extruded into fiber form through a diamond-wire die built into an apparatus exerting high pressure on the preform. The extrusion temperature is varied from 200-350 °C and the extrusion pressure is settled at a certain point so that an extrusion rate of several centimeters/minute can be realized. The surface of the fiber prepared by extrusion is observed to be basically smooth, except that it may have a few scratches 1-2 μm wide [5].

The *edge-defined film-fed growth* (EFG) technique is used for materials that do not form glasses or are difficult or impossible to extrude. This method forms single crystal fiber

at a rather slow rate [10]. Single crystal fibers have been grown from *AgBr*, *CsI*, and  $Al_2O_3$  (sapphire).

Bridges, et al, [25] performed experiments with *AgBr*. A diagram of their fiber crystal-growing apparatus is shown in Figure 11 (b). Fiber growth occurs near the end of a nozzle that determines the size and cross-section of the crystal. The nozzle terminates one arm of a fused-quartz *U* tube that holds the liquid charge which is kept molten by a surrounding oven. The rate of liquid feed to the nozzle can be controlled by  $N_2$  gas pressure applied to the other arm of the *U* tube. A small oven around the nozzle tip has adjustable temperature and a water cooled element. Adjusting these two in position enable the melt-solid interface to be accurately positioned. Bridges, et al, were able to grow fibers with the size determined by both the outside diameter and inside diameter of the nozzle. (This is shown in the inset of Figure 11 (b).) Clear, smooth fibers with diameters between 0.35 and 0.75 mm have been grown at rates up to 2 cm/min. Theory predicts that the allowable growth rate is inversely proportional to the cross-sectional area of the crystal. Provided that the thermal and mechanical conditions are sufficiently under control, there appears to be no limit to the length obtainable [23].

### ***3.5 Comments on Infrared Fibers***

The possibility of ultralow losses in infrared fibers leads to the possibility of communication systems with repeater spacings greater than 1000 km. In order to take advantage of this, the fibers need to be single-mode with low dispersion. The refractive index profile is an important feature to consider in design procedures to achieve this low

dispersion as well as low microbending loss. It is also desirable to match the coefficients of expansion, the viscosities, the glass transition temperatures  $T_g$  and crystallization temperatures  $T_c$  of the core and cladding materials [27]. (Crystallization occurring at the core/cladding interface is a major problem with zirconium fluoride based fibers.) Note, however, that materials with the same wavelength of minimum loss have nearly the same properties.

Bending and microbending losses cannot be treated separately from the dispersion shifting requirements at long wavelengths [27]. This leads to materials and processing problems. The large  $\Delta$ 's needed at longer wavelengths cause an increasingly larger mismatch in the properties of the core and cladding materials, which may in turn cause an increase in interface scattering. Also, the complicated (at least more so than a step) index profiles needed to keep dispersion shifted propagation with large  $\Delta$ 's would require more complicated fabrication methods as compared to the procedures available to create the step-index profile.

Some researchers [28] believe that materials problems are slowing down any advances in infrared fiber technology. It is not yet known what materials are best for any given application. Purification and stability are major concerns, as well as extrinsic absorption (which remains the limiting factor). Others argue that the problem lies in fabrication procedures. "Alternative glass preparation" methods are needed, especially to increase material purity.

## *3.6 An Application*

This chapter has presented an overview of infrared optical materials and fibers. One particular application for these fibers is noncontact temperature measurement. Several authors [29, 30, 31, 32] have experimented in this area and have achieved favorable results. Their specific research will be discussed in the following chapter, which describes many different types of fiber optic temperature sensors.

Specifically, the infrared-transmitting fibers discussed in this chapter would allow transmission into the infrared, and thus allow multi-wavelength pyrometers having wavelengths there. The types of infrared fibers discussed here could specifically be used for pyrometry over long distances because the attenuation is, in principle, so low. Applications (aluminum or steel plant monitoring, or drop tube monitoring, for example) that intrinsically require tens or hundreds of meters of fiber--owing to the physical layout of the plant or tube, require low attenuation such as is available with infrared fibers. Silica-based fibers simply will not work. The review of infrared optical fibers presented in this chapter is directly applicable to the following chapter on temperature sensors because different types of fiber materials, as well as different fabrication methods, are best suited to specific applications.

## 4.0 Fiber Optic Temperature Sensors

Several types of optical fiber temperature sensors have recently been developed, each based on a slightly different principle. Such principles include phase, wavelength, polarization, and intensity modulation. Other categories include point and distributed sensors, as well as contact and noncontact sensors. Point sensors measure the specific parameter at a certain point, whereas distributed sensors measure the parameter along the length of the fiber. Contact sensors, as the name implies, need to actually touch the object under examination, and noncontact sensors do not. The fiber itself may be the sensing medium, or act as a lightguide to and from another transducer element [33]. This chapter presents several different types of fiber optic temperature sensors and compares sensing mechanisms and sensor performance. It is not, however, an exhaustive survey.

## 4.1 Interferometric Sensors

In an all-fiber sensor, a temperature change  $\Delta T$  induces a phase shift  $\Delta\phi$  in the light propagating in the fiber due to two effects: the change in the length of the fiber due to thermal expansion or contraction, and the temperature-induced change in the index of refraction. This phase shift is given by

$$\frac{\Delta\phi}{\Delta T} = \frac{2\pi L}{\lambda} \left( \frac{n}{L} \frac{dL}{dT} + \frac{dn}{dT} \right), \quad (4-1)$$

where  $\phi = \frac{2\pi nL}{\lambda}$  and  $L$  is the length of the fiber [34, 35]. The phase shift can be readily determined with an interferometer. If, in the temperature range of interest, the phase change is proportional to the temperature change, then the temperature change can be calibrated easily in terms of the phase change [36]. Even if the phase change is not proportional to the temperature change, calibration is possible but more difficult.

Interferometers can basically be constructed in one of two ways [37]: first, by using two fibers, each carrying one mode, and exposing one fiber to the temperature change and using the other fiber as the reference; second, by using one fiber that carries two modes whose phase delays have different responses to the temperature change. The major advantage of a one-fiber interferometer is that all of the interfering modes see the same temperature; hence, common mode rejection is high. Strong responses for interferometers are only obtained when the temperature (or any force to be investigated) affects the modes differently.

### 4.1.1 Mach-Zehnder Interferometers

Figure 12 shows a Mach-Zehnder interferometer that has single-mode optical fiber for the two arms. If the optical pathlengths of the arms are approximately equal, the light from the two fibers interferes and forms a series of bright and dark fringes. A change in the relative phase of the light from one fiber with respect to the other is seen as a displacement of one fringe [35]. When the phase of light leaving the fibers changes (if, for example, one fiber is subject to a different temperature than the other), the difference appears as a displacement of fringes. The phase difference can be measured from this displacement.

Hocker [35] theoretically calculated a fringe displacement of 17.0 fringes /°C –m of fiber. Experimentally, however, he arrived at  $13.2 \pm 0.5$  fringes /°C –m. The discrepancy is due to the materials making up the fiber: the theoretical calculation was for pure  $SiO_2$ , while the experimental results were for a doped  $SiO_2$  core fiber.

There are several problems with a Mach-Zehnder sensor [38]. First, the reference arm must be kept free from any external temperature change, otherwise the phase of the reference signal will be affected by the temperature change around the reference fiber arm. Second, both arms should see the same pressure conditions; if not, the output is affected by the difference of the total pressure variations in both arms. It also has specific alignment requirements. Lastly, the measurement is of the change in the *average* temperature of one fiber arm with respect to the other. It is difficult to satisfy all of these requirements in most practical applications of this sensor type.

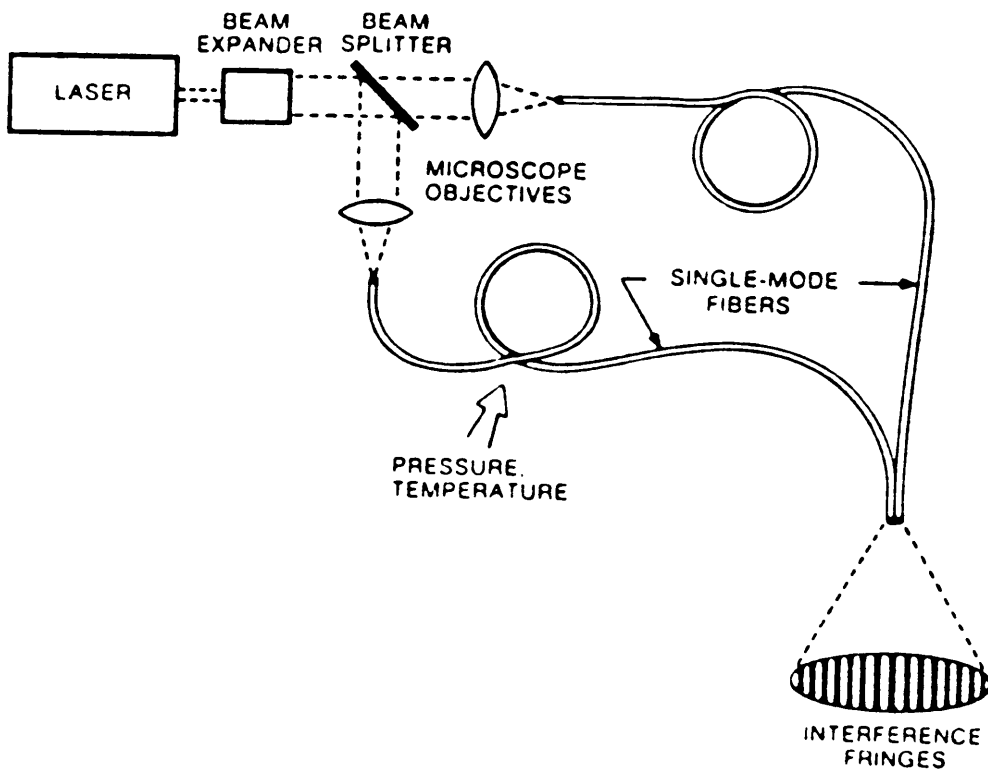


Figure 12. A Mach-Zehnder Interferometer [35]

## 4.1.2 Michelson Interferometer

The simplest form of interferometer is the Michelson interferometer. It is shown in Figure 13. Note that the fiber is single-mode. Once again, the close coupling of the two fibers provides much common mode rejection, therefore reducing the effect of environmentally induced perturbations.

In regard to equation (4-1), note that in the Michelson interferometer the optical signal travels through the sensing element twice, so that  $L$  is twice the physical length of the sensing element [39]. Over 95 percent of the thermally induced phase shift is due to the change in index of refraction for uncoated silica fibers [35]. Hence, in order for thermal expansion to significantly contribute to  $\Delta\phi$ , the sensing fiber must be bonded to a material with a large coefficient of linear expansion.

Corke, et al, [39] devised a frequency-stabilized Michelson interferometer with a temperature resolution of approximately  $1 \text{ m}^\circ\text{K}$ . They reduced frequency problems (laser jitter, drift in heat sink temperature, battery drain) by locking the emission frequency of their diode laser to an external Fabry-Perot cavity. Martinelli [40] has devised a new phase-compensation technique that offers an unlimited dynamic range. His method can be used in a system for the measurement of large but slowly time-dependent temperature change. He uses a form of Michelson interferometer with a phase-demodulation system based on a rotating half-wave plate retarder. The resulting temperature-induced phase shift was averaged at  $34.1 \text{ fringes}/^\circ\text{C}-\text{m}$ . (Note that this number accounts for the double passage of light through the sensing fiber and for a random phase that is added or subtracted during the measurement time.)

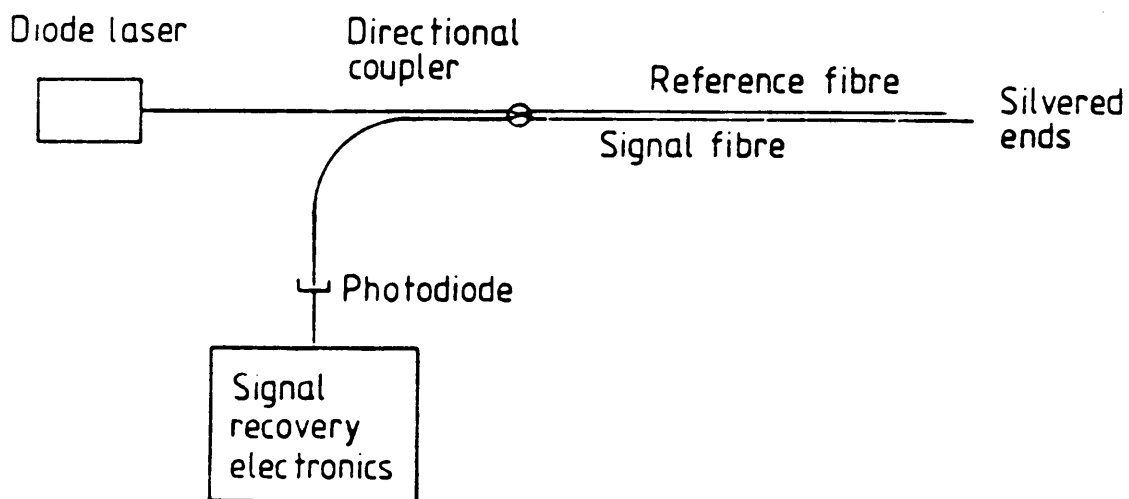


Figure 13. A Michelson Interferometer [39]

### 4.1.3 Wavelength-Modulated Interferometers

McMillan and Robertson [41] implemented a scheme that combines single fiber interferometry and wavelength modulation to determine temperature. The advantages of one-arm interferometry have been briefly discussed. There are also several advantages in measuring chromatic dispersion transmission spectrum rather than intensity: wavelength measurements can be performed with extreme accuracy and high resolution, absolute measurements can be made, and no intensity calibration is required [41].

The experimental set-up is shown in Figure 14. The fiber output shows the two-lobe pattern of one of the modes of the  $LP_{11}$  mode group. By using polarized light and introducing an offset at the launch, McMillan and Robertson could select one mode. Then they selected one lobe with a form of spatial filter.

Light propagates in the  $LP_{01}$  and  $LP_{11}$  modes of the fiber. Interference is in the form of an intensity contrast between the two lobes of one of the modes in the  $LP_{11}$  mode group in the near field of the output. It will occur if the delay difference between the modes is less than the coherence time of the light. If this delay difference is varied, power will oscillate between both lobes [41]. The delay difference can be changed by changing the fiber  $V$  number, index of refraction, or length. McMillan and Robertson showed the  $V$  number dependence by measuring the chromatic transmission spectrum of one lobe. By changing the temperature, each of these three parameters will vary. Thus, one would expect to see changes in the chromatic transmission spectrum and variations in transmitted power, in one lobe, as a function of temperature [41].

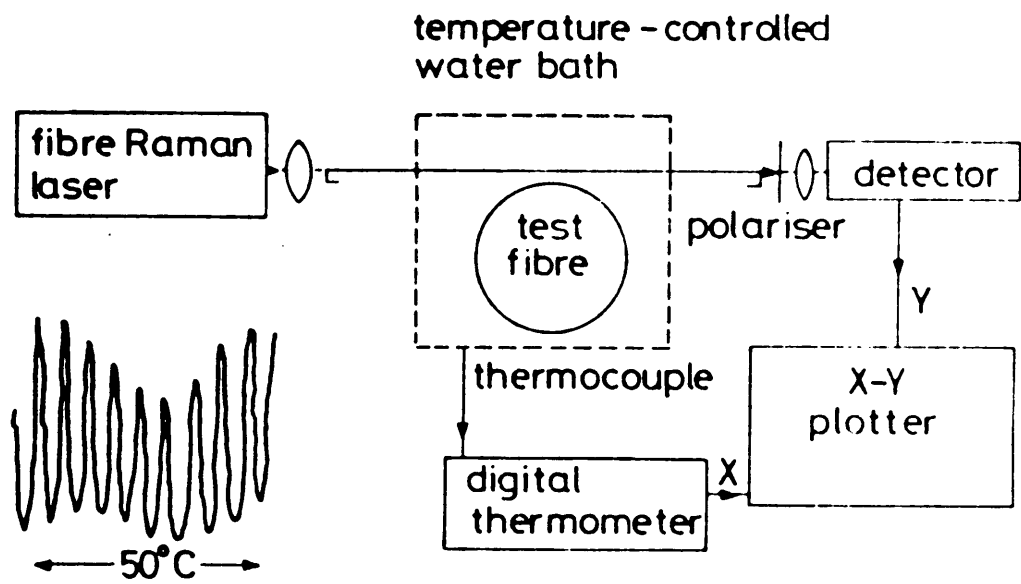


Figure 14. A Wavelength-Modulated Interferometer [41]

The temperature dependence of the one-lobe power was measured at three wavelengths, with temperature varying from around 10 to 60 °C . The temperature sensitivity varied from 0.03 fringes/ °C -m at 1.034 μm to 0.07 fringes/ °C-m at 1.124 μm. The separation of adjacent fringes about a fixed wavelength was measured at 20 and 60 °C. It gave a result of about 0.1 nm /°C – m. Generally speaking, wavelength measurements can be performed with high resolution and accuracy, so they are often preferable to intensity measurements. The wavelength spacing of fringes demonstrates that wavelength detection is a possibility for dual-mode sensors [41].

#### **4.1.4 Polarimetric Interferometers**

Polarization sensors are based on changes in the birefringence of single-mode fibers [34]. They exploit the temperature-dependent change in phase delay between the orthogonal eigenmodes of highly birefringent fiber, such that the temperature modulates the state of polarization of the guided laser beam. These sensors offer a greater unambiguous measurement range. However, this increase in range is only achieved with a proportional reduction in resolution [42]. One advantage of this type of sensor is that the light is confined within a single fiber and polarization components are simpler in principle than those required for otherwise based interferometers.

A one-arm interferometer with birefringent fiber solves some of the problems associated with the Mach-Zehnder interferometer [37, 38]. It utilizes the principle of the difference in temperature-dependence of the propagation constants between two orthogonal modes of the birefringent fiber. The sensitivity of this interferometer is lower than that of the Mach-Zehnder, but it has two advantages. First, the temperature of the reference arm

does not need to be severely controlled. This leads to simple construction. And it is insensitive to isotopic pressure variations when made of birefringent fibers with high internal stress. Eickhoff's [37] one-arm interferometer was based on the direct measurement of the phase shift of the interference light intensity.

Corke, et al, [39] studied temperature induced changes in the modal birefringence of short length of bow-tie polarization preserving fiber. They excited only one eigenmode in the system. The change in the modal birefringence of the sensing fiber is monitored by using the unused polarization mode of the input fiber as a polarization analyzer. They showed that the input fiber was insensitive to temperature changes. This was due to the effective polarization isolation of the light as it propagates in the fiber. They counted fringes to determine the temperature change, but were unable to obtain the direction of the change. Their polarimetric sensor turned out to be 50 times less sensitive than their Michelson interferometer. However, it is much simpler to construct and can be used in hazardous environments that do not require a high resolution temperature measurement [39].

Two years later, Leilabady, et al, (including Corke) devised a new configuration that yielded the high resolution of the conventional interferometer combined with the wide measurement range of the polarimetric device [42]. They used highly birefringent fiber as the sensing element. It was set up to form an interferometer with amplitude-modulation at the input end of the fiber, and reflection at the far end. The polarization components used allowed each of the two optical outputs to be associated with one of the two orthogonal linear polarization modes of the fiber. Therefore, the fiber was actually equivalent to two interferometers, with each one corresponding to the orthogonal polarization eigenmodes.

Figure 15 shows the experimental set-up. The eigenmodes of the fiber were equally excited. The ends provided low reflectivity mirror faces that were normal to the fiber axis. A small part of the input power is reflected from the input face, but most of it is guided to the far end where again a fraction of the power is reflected. These two reflected beams mix coherently and are partially reflected by the beam splitter to the half-wave plate. The half-wave plate is adjusted so that the polarization eigenaxes of the fiber and of the beam splitter coincide. The beam splitter divides the beam so that the components of each fiber eigenaxis is incident on a different detector. The piezoelectric cylinder was to allow for phase modulation, which in turn eases the signal processing. 70 mm of the fiber was enclosed in a furnace [42].

Their results are as follows [42]. Larger or smaller sensing lengths can be used to yield greater or lesser resolution with a narrower or wider measurement range. The dynamic range, however, remains the same. It is dependent on the properties of the fiber and the phase resolution of the interferometer and signal processing systems. The dynamic range may be increased by using fibers with a smaller temperature dependence of  $\Delta n$ , or by using fibers with smaller values of  $\Delta n$  (that is to say, increased beat length). But longer beat lengths reduce the polarization holding properties of the fibers, due mainly to extrinsically induced birefringence. Leilabady, et al, increased the dynamic range by a factor of 20 over conventional interferometers without resolution loss. They separately recovered the optical phase change of each interferometer and the differential optical phase change induced by a physical change inside the fiber. They were successful in combining the advantages of the interferometric and polarimetric sensors.

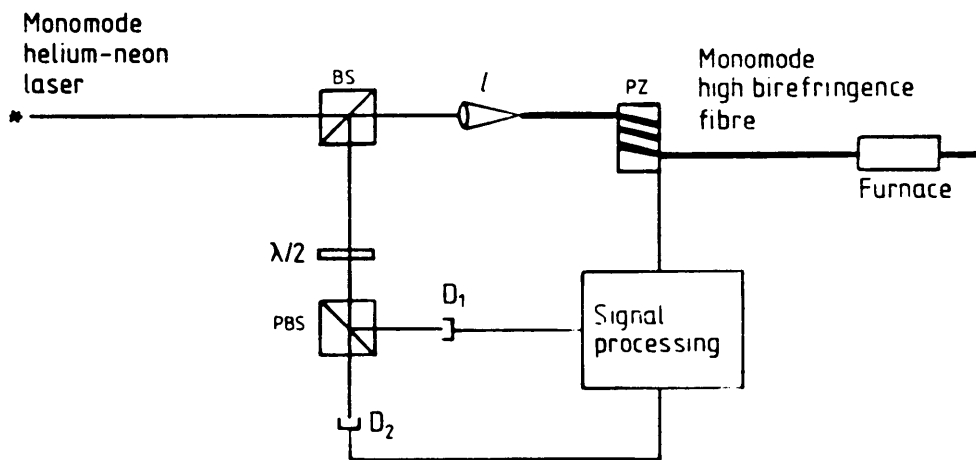


Figure 15. A Polarimetric Interferometer [42]

### 4.1.5 Fabry-Perot Interferometers

A fiber optic Fabry-Perot interferometer is a piece of single-mode fiber with the ends coated to form reflective surfaces. As in any interferometric set-up, a change in optical path length due to temperature changes can be determined by watching the interference of the fields. Unfortunately, however, usually the direction of the temperature change cannot be determined. More information than the fringes is needed. Tseng and Chen [36] proposed a technique to determine the temperature change and its direction by using a Fabry-Perot optical fiber sensor.

To sense the direction of temperature change, the Fabry-Perot cavity is divided into a sensing section and a reference section [36]. The phase delay in these sections is  $\phi_s$  and  $\phi_r$ , with the total phase delay being  $\phi = \phi_s + \phi_r$ . Let  $\phi_r$  vary in a specific and periodic fashion with period  $\tau$  (namely, a triangle waveform). This change is a known quantity and is used as a reference. It can be achieved by changing the index of refraction and/or the length of the reference fiber section or light frequency. Next, by recording output fringes, the time separation between consecutive peaks or valleys in the first and second half periods,  $t_1$  and  $t_2$ , and the time between peaks or valleys in the first and second half periods,  $t_1$  and  $t_2$ , can be determined. Let  $\Delta\phi_r$  and  $\Delta\phi_s$  be the net phase shifts between consecutive interference peaks for the reference and sensing phase delay. With no temperature change,  $\Delta\phi_s$  is zero. If the temperature there does change, a phase shift  $\Delta\phi_s$  is superimposed onto  $\Delta\phi_r$ . The absolute value of the time rate of change of  $\Delta\phi_r$ , as well as that of  $\Delta\phi_s$ , in both half periods can be readily calculated. After the phase changes due to the temperature change alone in  $t_1$  and the phase changes due to the temperature change alone in  $t_2$  are calculated, the temperature change and direction of the change can be determined by the manipulation of six equations.

Tseng and Chen obtained a temperature of 0.305 fringes /°C –cm. They used a PZT cylinder to elongate the fiber.

#### 4.1.6 Cross-talk Interferometer

The cross-talk fiber optic temperature sensor described here is a differential interferometer, whose interfering modes propagate in the same fiber. Hence, a reference fiber is not needed. It is based on the thermal dependence of cross-talk between closely spaced cores within one cladding. Since a thermal perturbation will influence the coupling between the cores, it can be sensed by illuminating one core at one end of the fiber and observing the change in the light distribution in all cores at the other end of the fiber. In a two-core fiber, light will switch back and forth between cores as the strength of the perturbation is changed [43].

Meltz, et al, [43] worked with such sensors. To begin, consider some of the theory. In a twin-core fiber, energy in cores is completely exchanged in a beat length  $\lambda_b$ . The change in intensity in each core along length  $L$  is a periodic function of the beat phase  $\phi = \frac{\pi L}{\lambda_b}$ . The energy exchange can be analyzed in terms of modal interference. Twin-core normal modes are approximately linear combinations of the lowest order  $HE_{11}$  single-core excitations. If another core is present, the  $HE_{11}$  mode is split into two other modes with slightly larger and smaller propagation constants. The splitting is greater for closer spaced cores and smaller  $V$  numbers. To obtain cross-talk, the  $V$  number must be greater than the cutoff for the antisymmetric combination of  $HE_{11}$  modes, but less than 2.405 to avoid propagation of the next higher-order modes.

With these twin-core sensors, a periodic variation in the output core contrast is seen when one core is illuminated and the temperature is either increased or decreased. The change in light distribution can be related quantitatively to a change in the coupling between cores, which is due to effects of linear expansion and refractive index variation [43].

The twin-core fiber's response to temperature varies. This is in part because the coupling between cores is changed by a shift in the  $V$  number. The sensitivity (which is due almost entirely to the linear expansion of the core and the thermo-optic effect) can be optimized by choosing an appropriate core size or wavelength for a given  $NA$  and core spacing. By proper selection of materials and fiber geometry, cross-talk can be made almost temperature independent. The temperature sensitivity at a certain wavelength can be determined from a measurement of  $\frac{\Delta\phi}{\Delta\lambda}$ . This wavelength sensitivity is a direct indication of the change in coupling factor with  $V$ , and therefore temperature [43].

A twin-core cross-talk temperature sensor can be designed to detect very small temperature changes. It can come to within two orders of magnitude of the sensitivity of a fiber optic Mach-Zehnder or Michelson interferometer with one leg held at a constant temperature. A multi-core sensor will have a greater unambiguous range than a twin-core fiber of equal length and sensitivity.

## 4.2 Fluorescence-Based Temperature Sensors

Grattan, et al, [44] developed a point sensor that uses the temperature-sensitive absorption properties of doped glass. The absorption edge of the glass is sensed using a LED source at 820 nm, which overlaps the edge. They used a novel approach for a reference wavelength for several reasons: first, to avoid the problems of differential transmission of a sensing wavelength and a reference wavelength through the fiber; second, for coupling and connector problems; and last, for remote problems with launching light from two LEDs into the fiber. The new approach was to generate a wavelength at the sensor itself by inducing fluorescence in a small piece of neodymium doped glass that was bonded to the first piece of doped glass. The wavelength chosen for the sensor was one which corresponds to a strong absorption in neodymium. Fluorescence at 1.06  $\mu\text{m}$  is produced when a small amount of incident radiation is absorbed. The intensity of fluorescence produced is independent of a 300  $^{\circ}\text{K}$  temperature range. Therefore, a "self-referencing" system is utilized with the wavelength produced separated enough to allow a wide working temperature range [44].

Figure 16 shows this sensor. The fiber used was 600  $\mu\text{m}$  in diameter. All parts were placed in a small stainless steel container. An upper limit is set on the use of the sensor because the softening point of the neodymium doped glass is around 400-500  $^{\circ}\text{C}$ . There is a weak fluorescence by the neodymium at 880 nm, but it is quickly reabsorbed by the highly doped glass. Fluorescence at 1.3  $\mu\text{m}$  is past the sensitivity of the detector they used.

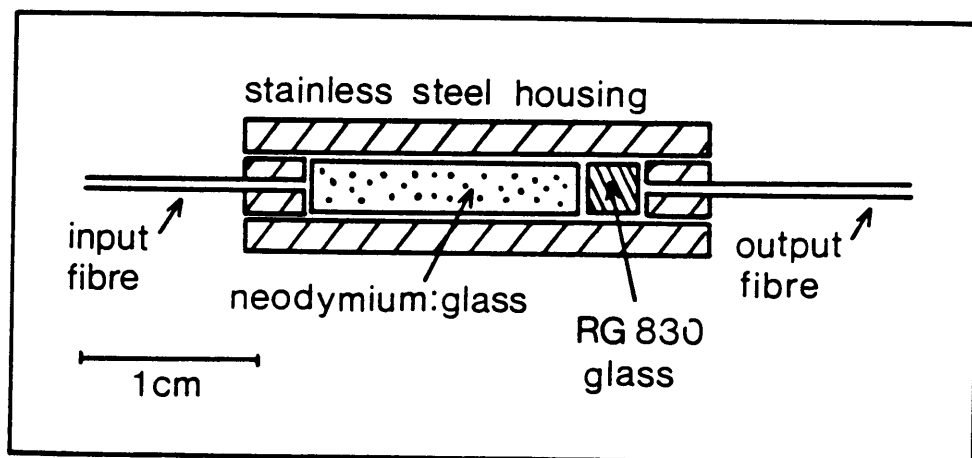


Figure 16. A Fluorescence-Based Temperature Sensor [44]

The electrical part of their system detected and separated the transmitted sensing signal and fluorescence reference signal, took a ratio of their relative intensities, and matched them with a calibration [44].

They concluded that the fluorescence referencing technique was an accurate method of monitoring the actual signal level at the sensor element. It allowed for variations in input light level, and was tested between 20 and 130 °C [44].

Previous work by the same authors [33] demonstrated the use of luminescent (light-emitting) properties of a fluorescent element alone as a temperature sensor. It was based on the principle of the change in "decay-time" of the fluorescence of neodymium doped glass that had been excited by infrared radiation from a LED. The decay time is hundreds of microseconds, so it can be measured accurately with available electronics. And it eliminates the need to make an accurate measure of, and then reference to, the input light intensity.

They observed an exponential decay of the emission over a period of two lifetimes. This led to obtaining a temperature value to an accuracy of  $T \pm 3^\circ\text{C}$  in the temperature range studied [33].

Both of Grattan's studies used optical fibers as light guides to address the actual sensor head.

### ***4.3 Evanescent Field Absorption Sensor***

This is an example of an intensity modulated sensor. Falco, et al, [45] constructed a temperature sensor based on the temperature dependent absorption of a lossy liquid surrounding a polished fiber section.

A diagram of their sensor is shown in Figure 17. The fiber is single-mode, step-index, with core and cladding indices  $n_1$  and  $n_2$ . The plane of the polished fiber is a distance  $d$  from the core. Note that the fiber is embedded in a lossy medium with complex permittivity. The evanescent modal field will thus penetrate this medium.

No exact theory is available to study this structure [45]. Theoretical studies using planar multi-layered models have been undertaken. In calculating the attenuation coefficient, it was concluded that the permittivity and  $d$  terms were separable. Falco showed that the permittivity of the measured temperature was only dependent on the permittivity at the calibration temperature, the attenuation at the calibration temperature, and the attenuation at the measured temperature. Hence, the difficult to control parameter,  $d$ , can be eliminated.

The sensitivity of this device is 0.2 dB /°C and has a 50 ° dynamic range. The low sensitivity comes from the low indices of the lossy media used in the experiment. High sensitivity requires a medium with an index lower than, but close to, that of silica. In fact, in order to obtain a high sensitivity, this condition is even more important than having a high concentration of absorbing material [45].

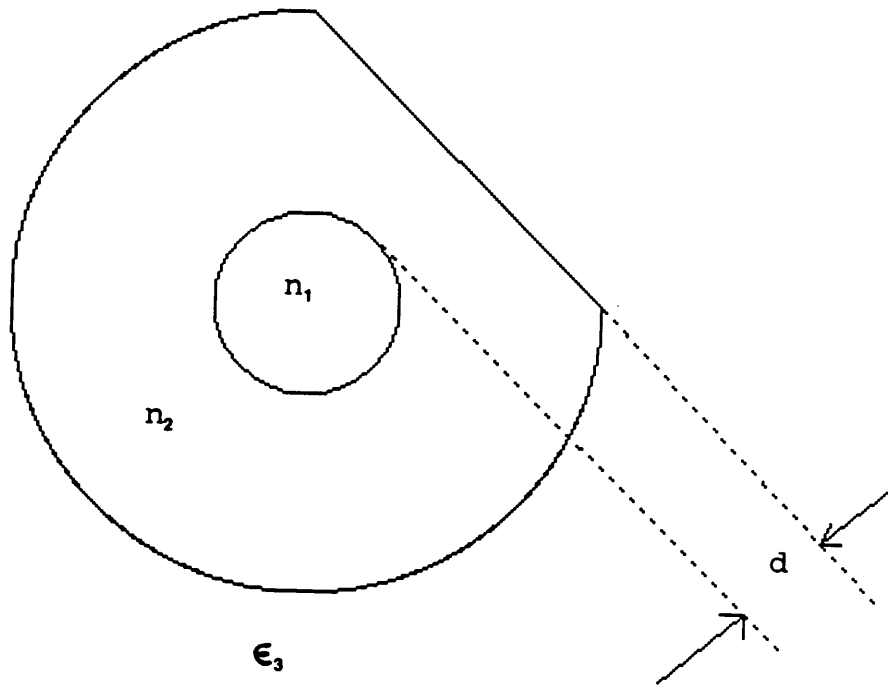


Figure 17. An Evanescent Field Absorption Sensor [45]

## **4.4 OTDR Temperature Sensing**

The optical time domain reflectometer makes use of the fact that microscopic fluctuations of the refractive index and small flaws in an optical fiber cause light to be reflected. Short pulses of light are injected into one end of the fiber and the signal is reflected (at those discontinuities) and observed at the input end. A scatterer is seen as a spike in the back reflected signal. Rayleigh scattering causes a continuously reflected, very low amplitude signal. Special electronics capable of identifying periodic signals that are embedded in noise are needed to detect this scattering [3].

The major strength of the optical time domain reflectometer is that it is able to distinguish between sections of the fiber showing different losses. And, of course, it is performed in real-time and continuously monitors a specimen [3].

### **4.4.1 Liquid-Core Fiber Distributed Temperature Sensor**

To be able to use optical time domain reflectometry (OTDR) in a fiber sensor, the fiber must be specially designed so that its backscatter signal is sensitive to the physical parameter to be measured. Sensors use changes in scattering loss,  $NA$ , or total attenuation to provide the required sensitivity [46]. Hartog [46] developed a temperature distribution sensor using liquid-core fibers. These fibers provide good immunity to mechanical perturbations and other external factors.

As the temperature of a liquid core fiber is increased, two major effects occur. First, the core refractive index decreases; thus the  $NA$  decreases, which leads to a reduction of the

backscatter signal. Second, the scattering loss increases due to the increasing thermal agitation. To make the sensor practicable, one of these effects must be eliminated. Hartog eliminated the effect of  $NA$  variation in the backscatter signal with a mode filter.

Figure 18 shows the experimental set-up for Hartog's distributed temperature sensor. Note that the launch fiber is inserted inside the core of the sensing fiber to form a joint. It then automatically selects modes bound to the core (since power in cladding modes traveling through the core always fall outside the  $NA$  of the launch fiber). Backscatter measurements were made on liquid-core fibers. The oscilloscope traces of these signals showed increases in signal level in positions corresponding to areas where the fiber was heated. The localized temperature increase was revealed, due mostly to the large backscatter factor of the liquid-core fibers.

Hartog showed that it is possible to build and operate these sensors very near to the theoretically predicted sensitivity. This guarantees that the sensitivity is reproducible from one sensor to another.

Since the loss of heated sections of the fiber is affected by attenuation of higher order modes, the question of the effect of differential modal attenuation (DMA) on the sensor was investigated [46]. It was found to be negligible provided that the fibers have low-loss claddings and that a mode filter was placed in front of the receiver. Negative effects of cladding modes can also be removed by using a mode filter and a lossy primary coating.

Hartog's analysis showed that his sensor was capable of 1 m resolution over fiber lengths of more than 100 m, with a temperature accuracy of 1 °C. The fibers used showed a sensitivity of  $2.3 \times 10^{-2}$  dB/°C over the range from 5-100 °C. The maximum operating temperature is the temperature at which the  $NA$  of the liquid-core fiber equals that of

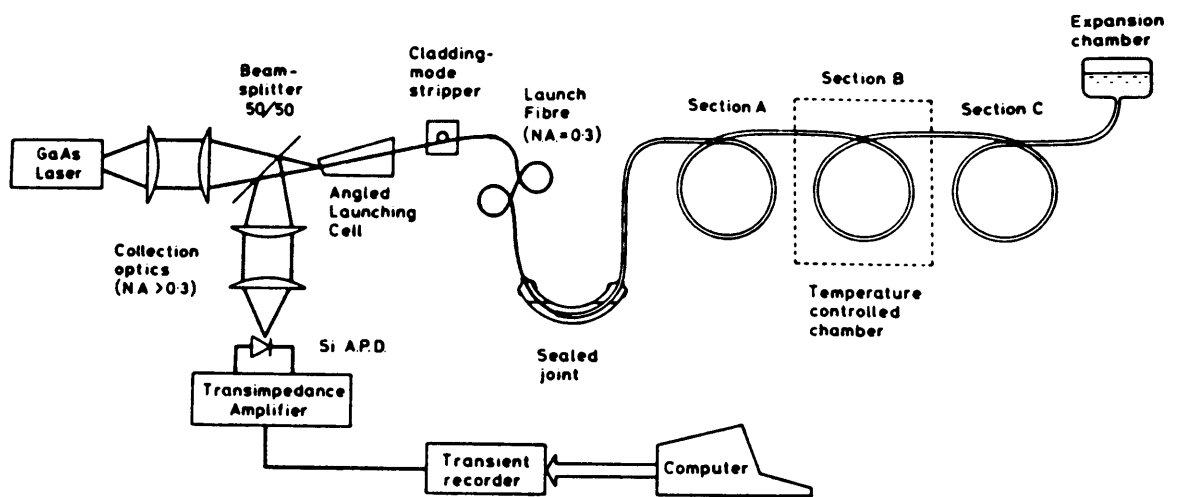


Figure 18. A Liquid-Core OTDR Sensing System [46]

the launch fiber. At low temperatures, the range is limited by the fiber loss that increases with decreasing temperature.

#### **4.4.2 Raman Ratio Temperature Sensing**

Before delving into Raman backscatter based OTDR temperature sensing, the Raman effect will be explained.

It can be observed when high intensity light passes through a solid or liquid. The emerging light beam contains new wavelength components in addition to those present in the incident beam. The longer wavelength components are called Stokes lines and the shorter wavelength components are called anti-Stokes lines. The Stokes lines are usually more intense [3].

In classical terms, the Raman effect can be stated this way: A strong incident light beam excites molecular vibrations in liquids and optical phonons in solids. These vibrating molecules then interact with the incident beam to form upper and lower sidebands of radiation. In terms of frequency, the upper sidebands are the anti-Stokes lines and the lower sidebands are the Stokes lines. In quantum-mechanical terms, the Raman effect is as follows: A pump (incident) photon is absorbed and then re-emitted, but part of its energy is used to excite the molecule taking part in the interaction to a higher vibrational state. Therefore, the re-emitted photon has lower energy and a longer wavelength, resulting in Stokes radiation. If the molecule was in an excited vibrational state before the interaction and is left in a lower vibrational state after the photon has been re-emitted with higher energy or shorter wavelength, then the result is anti-Stokes radiation [3].

A good medium for generating Raman light is an optical fiber. Although the Raman effect is not especially strong in glasses, the high light intensity and long interaction length of fibers make up for its naturally small Raman activity. Gain can also be observed at the Stokes wavelengths. High Stokes energy occurs by amplification of spontaneously emitted Raman light. In a long fiber, the "light power" can build up in a Stokes line so that there is almost complete conversion of the incident light to Raman light [3].

The ratio of anti-Stokes to Stokes scattered intensities is a function of temperature, so it is therefore an excellent parameter on which to base a temperature sensor [47].

$$R(T) = \left( \frac{\lambda_s}{\lambda_a} \right)^4 \exp\left( -\frac{hcv}{kT} \right), \quad (4-2)$$

where  $\lambda_s$  is the Stokes shifted wavelength,  $\lambda_a$  is the anti-Stokes shifted wavelength,  $h$  is Planck's constant,  $c$  is the velocity of light,  $k$  is Boltzman's constant, and  $T$  is the absolute temperature.

Two wavelength dependent effects, however, may alter the Stokes and anti-Stokes backscatter signals differently [47]. Material dispersion results in a small difference in group velocity between  $\lambda_a$  and  $\lambda_s$ . This will only be significant if very high spatial resolution is needed. The difference in attenuation between  $\lambda_a$  and  $\lambda_s$  could be more serious. It will progressively alter the Raman intensity ratio by a factor of  $\exp(\lambda_a - \lambda_s)z$  (where  $z$  is the length of the fiber) during the return path. Attenuation differences are most likely to be greater at short wavelengths since the Rayleigh scattering contribution to attenuation varies as  $\lambda^{-4}$ .

There is a similarity between Rayleigh backscatter based OTDR and Raman backscatter based OTDR. For Raman OTDR, the only additional equipment needed is a spectrometer to reject the Rayleigh scattered light and pass the Raman spectral components [47]. But only an ideal spectrometer and photodetection system will have equal sensitivities at  $\lambda_s$  and  $\lambda_r$ . A practical system will have sensitivities that differ by a factor,  $F$ , that must be taken into account when calculating temperatures. This can be achieved by measuring a reference section of the fiber which is at a known temperature,  $\Theta$ . If the measured Raman intensity ratios are  $R'(T) = F \cdot R(T)$  and  $R'(\Theta) = F \cdot R(\Theta)$ , then the unknown temperature  $T$  can be found from equation (4-3) below.

$$\frac{1}{T} = \frac{1}{\Theta} - \frac{k}{hcv} \ln \left[ \frac{R'(T)}{R'(\Theta)} \right] \quad (4-3)$$

Dakin, Pratt, et al, [47, 48] have used the Raman effect to determine the temperature distribution along an optical fiber. They used two experimental arrangements, as shown in Figures 19 (a) and (b).

Figure 19 (a) shows their argon ion laser system. They used 50/125  $\mu$  m, 0.2  $NA$ , graded-index fiber. Measurements with this system established that this method performs over a wide temperature range, 77-650  $^{\circ}K$ , and that repeatable readings are possible. Figure 19 (b) is their semiconductor diode laser system. The sensor fiber used was 100/140  $\mu$ m, which had the advantages of a large core for easy launching, and high  $NA$  for a good capture of backscattered light [48]. Due to its solid state source and detector, this system is more practical than the argon ion laser system. And even though the Raman backscatter is reduced at longer wavelengths, the fiber attenuation is lower, so that sensor lengths of over one kilometer are possible.

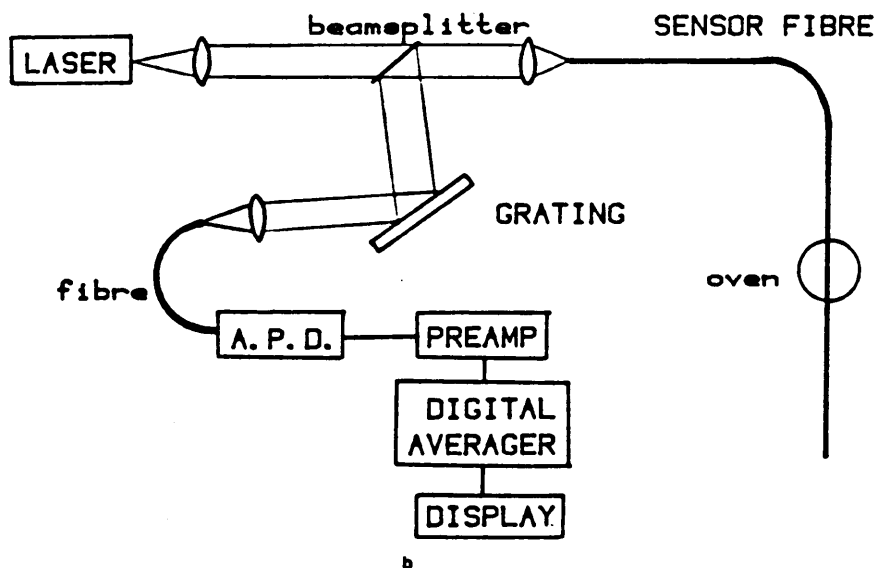
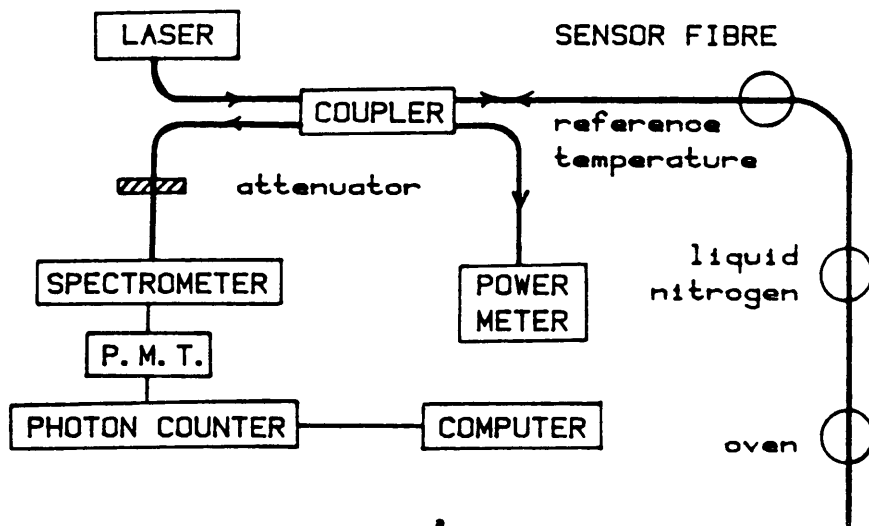


Figure 19. Raman OTDR Temperature Sensing Systems [47]: (a) Argon ion laser system (b) Semiconducter diode laser system

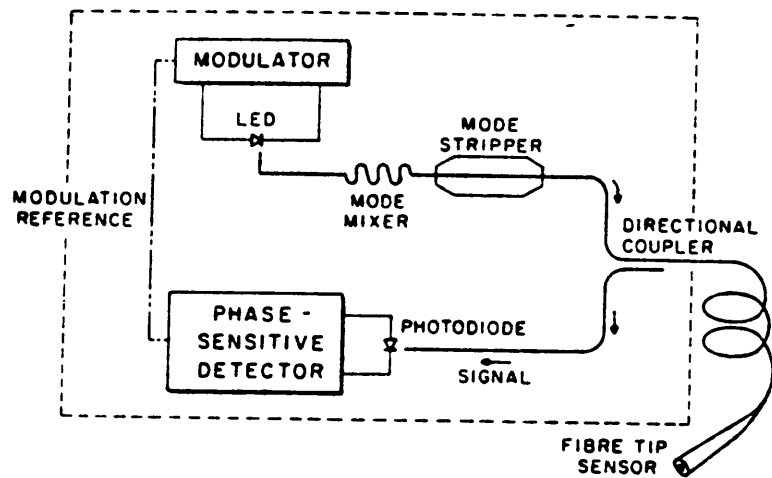
Farries [49] used the Raman effect to devise a point temperature sensor, as opposed to Dakin's and Pratt's distributed sensor. He used a probe, which can be any type of optical fiber. The sensor averages the temperature along the probe, and can cover a temperature range from -196 to 150 °C with an accuracy of 2 °C. If suitable coatings are applied to the fiber, the sensor can cover a range from almost -273 to 600 °C.

### *4.5 A Reflectometer to Sense Temperature*

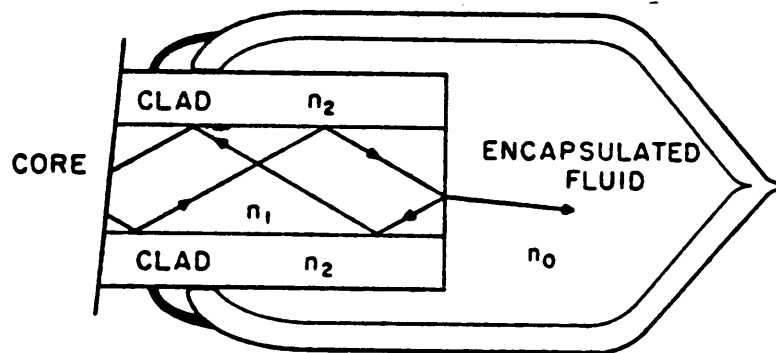
Legendre [50] has devised a temperature sensor based on Fresnel reflections occurring at sharp dielectric discontinuities. He encases an optical fiber in a volume of liquid that has an index of refraction that varies with temperature.

His apparatus is shown in Figure 20 (a). The mode mixer arrangement is to guarantee that all possible modes are excited, and then the mode stripper removes unwanted cladding modes. The fiber was 50/125  $\mu\text{m}$ . Figure 20 (b) shows the actual sensing probe. Clearly, the total reflection coefficient is dependent in  $n_1$ , but the temperature coefficient of  $n_1$  is so much smaller than that of  $n_0$  that changes in  $n_1$  can be neglected.

The sensitivity of the sensor depends on the signal-to-noise ratio and on the the response of the reflectometer to the changes in temperature. The temperature range is mostly determined by the characteristics of the fluid used; namely, freezing point, boiling point, and refractive index. As it varies with temperature, the refractive index of the fluid should never equal that of the fiber core. Legendre used ethylene glycol for the fluid in his experimental probe. His system operated over a range of 200 °C.



a



b

Figure 20. A Reflectometer to Sense Temperature [50]: (a) The sensor system (b) The sensing probe

## 4.6 Optical Fiber Pyrometers

Note that pyrometry will be thoroughly discussed in Chapter 5. However, since this chapter deals specifically with optical fiber temperature sensors, several examples of optical fiber pyrometers will be mentioned here.

In 1984, Artyushenko, et al, [29] reported studies on the use of KRS-5 fibers for pyrometric temperature measurement. The loss of these fibers is high in the short wavelength region of the spectrum and decreases with increasing wavelength in proportion to  $\lambda^{-2}$ . Therefore, these particular fibers can be used for *low* temperature measurements. The actual loss in the fibers they used was less than 1 dB/m in the 5-20  $\mu\text{m}$  range.

The apparatus they used was simple enough, consisting of a model blackbody, 0.5 mm diameter fiber up to 200 cm long with a 60 ° input angle, several infrared detection systems, an amplifier, and a chart recorder. A thermocouple was also attached to the chart recorder, for purposes of comparison. The lower limit on temperature measurements is set by the noise of the detector and amplifier system used. Different results were obtained with the different detectors. Obviously, the more sensitive the detector, the better the results.

Their system was operational from 50-400 °C. With refined electronics, it may be operational down to -100 °C. Artyushenko, et al, used this system for noncontact measurements of the temperature of printed circuit boards.

Rochereau [30] developed a fiber optic pyrometric sensor utilizing a silica (200/300  $\mu\text{m}$ ) fiber with the jacket removed. The bare fiber was placed in a stainless steel tube. In that arrangement, the sensor could be placed in front of a hot object or inserted directly into some material.

The fiber picks up radiation which is sent to an optoelectronic system. The signal is split into two channels by an achromatic optical fiber coupler. Each channel is defined, with the aid of silicon photodiodes with appropriate filters, by its specific spectral domain. The signals are then amplified, digitized, and processed.

Rochereau's pyrometer was operational from 700-1300  $^{\circ}\text{C}$ . The distance from the hot point to the sensor could not exceed 50 mm. Accuracy at 800  $^{\circ}\text{C}$  was 1 percent.

Zur, et al, [31] incorporated silver halide fibers into a simple radiometer. These fibers transmit well from 2-15  $\mu\text{m}$ , so they are also (as were Artyushenko's KRS-5 fibers) appropriate for low temperature measurements. The far end of the fiber was held a distance  $h$  from the body (an aluminum disc, in this case) whose temperature was to be measured. Results of the measurements did not vary as long as  $h$  was less than about 10 mm. It is theoretically estimated that the infrared fiber radiometer reading should be roughly independent of  $h$ . Zur, et al, made noncontact temperature measurements between 25-50  $^{\circ}\text{C}$ . There was good correlation between the radiometric results and a thermocouple reading. The minimum resolvable temperature was 0.1  $^{\circ}\text{C}$ .

Finally, Mordon, et al, [32] experimented in noncontact temperature measurements with zirconium fluoride fibers. They used two step-index fibers with different diameters; 450/550  $\mu\text{m}$ , and 200/250  $\mu\text{m}$ . For these fibers, losses between 1-4.5  $\mu\text{m}$  are below 1 dB/m. Infrared radiation from a blackbody was transmitted through 1 m lengths of each

of the fibers. A lock-in amplifier amplified the detectors' signals, and then those signals were processed as a function of controlled blackbody temperature. The transmitted signal was, of course, proportional to the core diameter of the fiber. The temperature range investigated was 60-150 °C. The output signal increased as the temperature increased, noticeably more so in the fatter fiber.

## **4.7 Summary**

This chapter has summarized current methodologies in the measurement of temperature using optical fibers. In the next chapter a novel alternative method is suggested which (a) simplifies the detection process, (b) employs in-line optical fiber signal processing devices (i.e., filters), and (3) uses fewer detectors and electronics than conventional systems.

## 5.0 Pyrometry: Theory and Experiment

A *radiation pyrometer* or *radiation thermometer* is a noncontact temperature-measuring device. As such, it can be used to determine the temperature of hot, moving particles.

### 5.1 Theory

Radiation temperature sensors operate with electromagnetic radiation whose wavelengths lie in the visible and infrared regions of the spectrum. They mainly utilize some part of the range 0.3-40  $\mu\text{m}$ .

All physical bodies may emit electromagnetic radiation or subatomic particles for a number of reasons. Regarding temperature sensing, we need only be concerned with that part of the radiation caused solely by temperature. Every body above absolute zero in temperature emits radiation dependent on its temperature. The ideal thermal radiator

is called a *blackbody* [51]. Planck's law governs this type of radiation, and is given in equation (5-1).

$$W_{\lambda} = \frac{C_1}{\lambda^5 [e^{C_2/(\lambda T)} - 1]} \quad [W/cm^2 \cdot \mu m], \quad (5-1)$$

where  $W_{\lambda}$  is the hemispherical spectral radiant intensity,  $C_1 = 37,413 [W \cdot \mu m^4/cm^2]$ ,  $C_2 = 14,388 [\mu m \cdot ^\circ K]$ ,  $\lambda$  is the wavelength of radiation  $[\mu m]$ , and  $T$  is the absolute temperature of the blackbody  $[^\circ K]$ . Equation (5-1) gives the distribution of radiant intensity with wavelength. A blackbody at a certain temperature emits *some* radiation per unit wavelength at every wavelength, but not the same amount at every wavelength. Figure 21 shows blackbody curves; that is, curves obtained from equation (5-1) by fixing  $T$  at various values and plotting  $W_{\lambda}$  vs.  $\lambda$ . Note that the curves show peaks at certain wavelengths, and the peaks occur at longer wavelengths as the temperature decreases. Hence, lower temperatures require measurement out to longer wavelengths. The shape of the curve can be shifted along the straight line connecting the peaks to obtain the curve at any temperature. The area under the curve is the total emitted power and increases quickly with temperature. Formulas for the peak wavelength  $\lambda_p$ , and the total power  $W_t$ , are

$$\lambda_p = \frac{2891}{T} \quad [\mu m], \quad (5-2)$$

and

$$W_t = 5.67 \times 10^{-12} T^4 \quad [W/cm^2]. \quad (5-3)$$

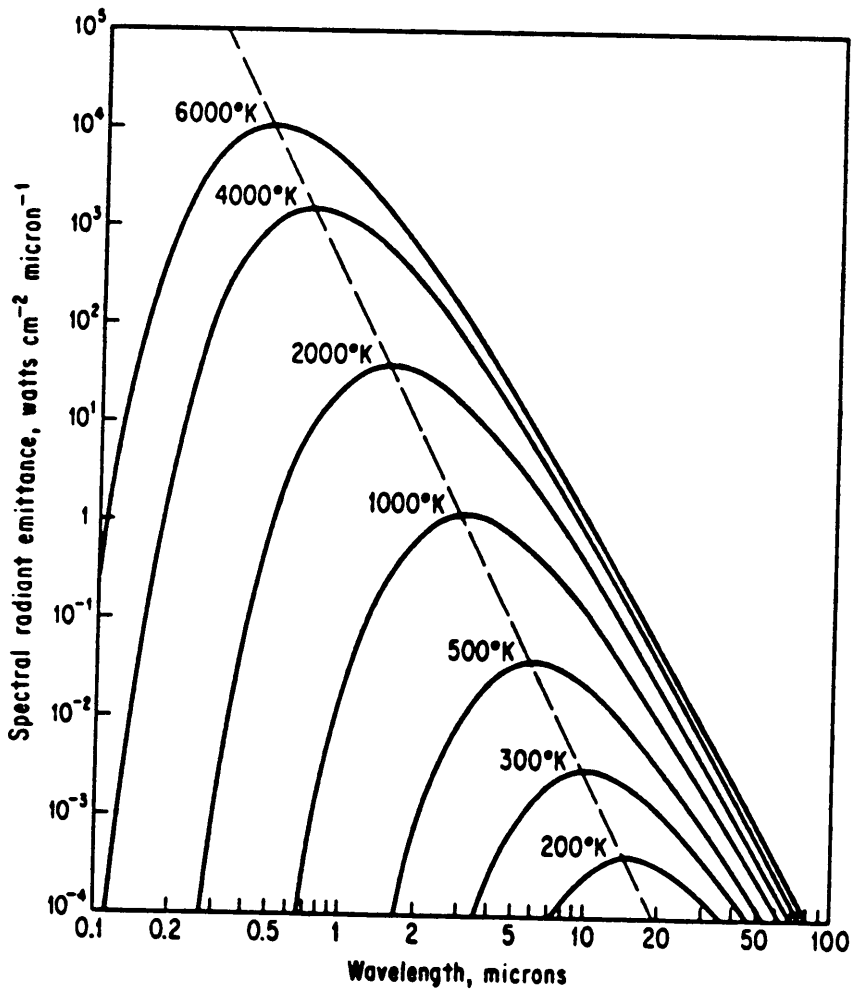


Figure 21. Blackbody Radiation Curves [52]

Equation (5-2) is known as Wien's displacement law. Equation (5-3) is known as the Stefan-Boltzman law, alternately written in the form

$$M = \varepsilon \sigma T^4, \quad (5-4)$$

where  $\sigma$  is the Stefan-Boltzman constant, and  $\varepsilon$  is the total hemispherical emissivity. Real body radiation deviations from blackbody radiation are expressed in terms of the emissivity of the measured body [51, 53].

If  $W_{\lambda a}$  is the *actual* hemispherical radiant intensity of a real body at temperature  $T$ , and  $W_{\lambda}$  is as defined as in equation (5-1), then the hemispherical spectral emittance  $\varepsilon_{\lambda, T}$  is defined as

$$\varepsilon_{\lambda, T} = \frac{W_{\lambda a}}{W_{\lambda}}. \quad (5-5)$$

For most cases,  $\varepsilon_{\lambda, T}$  varies with both  $\lambda$  and  $T$ . Then the radiation from a real body can be written as

$$W_{\lambda a} = \frac{C_1 \varepsilon_{\lambda, T}}{\lambda^5 [e^{C_2/(\lambda T)} - 1]}. \quad (5-6)$$

Similarly, the total power  $W_{\lambda a}$  of an actual body may be written as

$$W_{\lambda a} = C_1 \int_0^{\infty} \frac{\varepsilon_{\lambda, T}}{\lambda^5 [e^{C_2/(\lambda T)} - 1]} d\lambda. \quad (5-7)$$

If  $W_{\lambda}$  can be measured experimentally, then the hemispherical total emittance is defined by

$$\epsilon_{t, T} = \frac{W_{\lambda}}{W_t}. \quad (5-8)$$

Then, if  $\epsilon_{t, T}$  is known, the total power of a real body is given by

$$W_{\lambda} = 5.67 \times 10^{-12} \epsilon_{t, T} T^4. \quad (5-9)$$

If a body has  $\epsilon_{\lambda, T}$  equal to a constant for all wavelengths and a given  $T$ , it is called a *graybody*. For graybodies,  $\epsilon_{\lambda, T} = \epsilon_{t, T}$ , and the curves of  $W_{\lambda}$  vs.  $\lambda$  have exactly the same shape as for  $W_t$ . Since many radiation thermometers operate in a restricted band of wavelengths, the hemispherical band emittance has been defined as

$$\epsilon_{b, T} = \frac{\int_{\lambda_a}^{\lambda_b} \{\epsilon_{\lambda, T} [\lambda^5 (e^{C_2/(\lambda T)} - 1)]\} d\lambda}{\int_{\lambda_a}^{\lambda_b} \{1/[\lambda^5 (e^{C_2/(\lambda T)} - 1)]\} d\lambda}. \quad (5-10)$$

Notice that this is just the ratio of the actual and blackbody total powers within the wavelength interval  $\lambda_a$  to  $\lambda_b$  for bodies at temperature  $T$ . If the actual power can be measured directly,  $\epsilon_{b, T}$  can be found without knowing  $\epsilon_{\lambda, T}$ . For graybodies,  $\epsilon_{b, T} = \epsilon_{t, T}$  [51].

Now let us look specifically at pyrometry.

There are three basic classes of radiation pyrometers, namely , total radiation, brightness, and two-color or ratio pyrometers [54]. The last type can be made relatively independent of variations in emissivity. And since errors due to inaccurate emittance values are a problem in all radiation type temperature measurements, this method proves quite useful.

The basic concept requires that  $W_{\lambda}$  be determined at two different wavelengths and then the ratio of these two  $W_{\lambda}$ s be taken as a measure of temperature. For usual conditions of practical applications (for  $T$  less than about 4000 °C ), the terms  $e^{C_2/(\lambda T)}$  are much greater than 1.0, so that with close approximation

$$W_{\lambda_1} = \frac{\epsilon_{\lambda_1} C_1}{\lambda_1^5 e^{C_2/(\lambda_1 T)}} \quad (5 - 11)$$

and

$$W_{\lambda_2} = \frac{\epsilon_{\lambda_2} C_1}{\lambda_2^5 e^{C_2/(\lambda_2 T)}}, \quad (5 - 12)$$

where  $\epsilon_{\lambda_{1,2}}$  is the emittance of the target at wavelength  $\lambda_{1,2}$ . Then,

$$\frac{W_{\lambda_1}}{W_{\lambda_2}} = \frac{\epsilon_{\lambda_1}}{\epsilon_{\lambda_2}} \left( \frac{\lambda_2}{\lambda_1} \right)^5 e^{(C_2/T)(1/\lambda_2 - 1/\lambda_1)}. \quad (5 - 13)$$

Since  $\epsilon_{\lambda_1} = \epsilon_{\lambda_2}$  for a graybody, equation (5-13) becomes independent of emittance (as long as it is numerically the same at  $\lambda_1$  and  $\lambda_2$ ) [51].

## 5.2 Experiment

The specific problem considered here is to determine the temperature of a particle of a hot (500-3500 °C), molten alloy falling down an evacuated drop tube. The particles are 3-5 mm in diameter and their emissivities are unknown in general. There is one other requirement: the temperature measurement system must utilize optical fibers.

Since the particle is moving quickly down a tube, the sensor will have to be the noncontact type. And since the emissivity is unknown, the logical choice of sensor design appears to be a ratio pyrometer.

The original plan was to develop and implement an optical fiber ratio pyrometer using infrared fibers. The purpose of the infrared fibers was to be able to receive optical signals over a wider wavelength range than with silica fibers. (Recall that the transmission spectrum of silica fiber cuts off at around 2  $\mu\text{m}$  [29].) Of course, the first step would be to perform a "proof-of-principle" experiment, demonstrating the proposed technique in the laboratory. Once a model is operational, a real system can be implemented on the drop tube.

At first the idea of a straight, two-wavelength pyrometer seemed adequate. We would use an adjustable white light source (a Philips tungsten-halogen lamp) as the hot particle (as the current is increased, the brightness increases, hence the temperature increases), and take intensity measurements at two specified wavelengths, using narrow bandpass filters. Two detectors would be needed. Data could be compared to graybody curves and the temperature could be determined. Particle velocity could be simulated with a shutter.

However, while waiting for the detection equipment to arrive, we decided that only taking two data points over such a narrow range would be a waste of optical energy. It would be hard enough to couple an appreciable amount of white light into a fiber (not yet even accounting for the fact that the object is moving) without filtering most of the coupled energy away, and then splitting it for two detectors.

Hence, we started on a new approach, and decided to try to use all the captured optical energy we possibly could, first, by using high and low pass filters. The ratio of the energies collected at two detectors could be a single-valued function of temperature. Another scheme would use a "dual window" detector, which is a filter in itself, instead of using two detectors. This would certainly make use of the total available signal. One other choice was to use two detectors again, but to use their responsivities to determine a unique ratio-type of function. Figures 22, 23, and 24 show some of these filtering options.

Our final suggestion is to implement an in-line optical fiber filtering function which would feed a single optical detector. Among the advantages of this concept are the following: (a) only one detector is needed, in principle, (b) the filtering could be accomplished using either a grin lens - filter - grin lens system, or the fiber itself as the wavelength-filtering device, and (c) this may, somehow, allow for different particle emissivities (that is, different wavelength-filtering functions may be used for different alloys). Figure 25 depicts such an instrumentation scheme.

A model of the operation of the system shown in Figure 25 is given in equation 5-14.

$$S(\lambda) = W(\lambda) * T(\lambda) * R(\lambda) * F(\lambda), \quad (5 - 14)$$

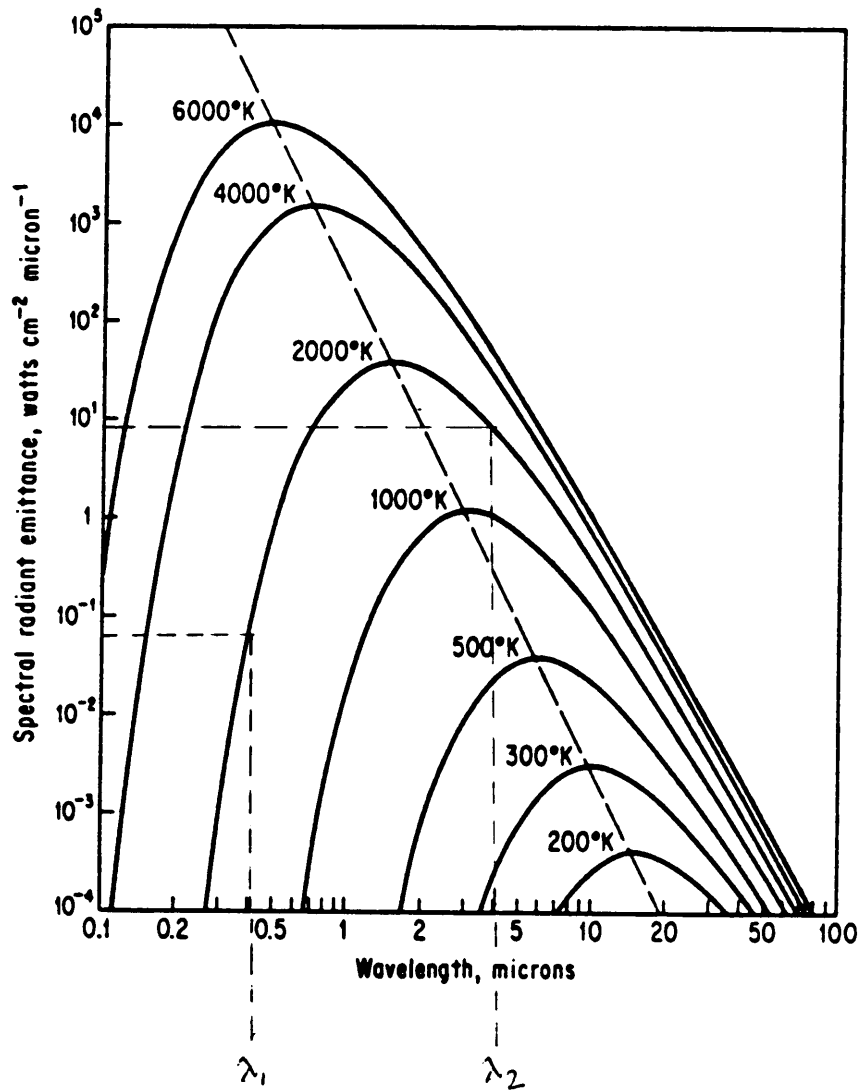
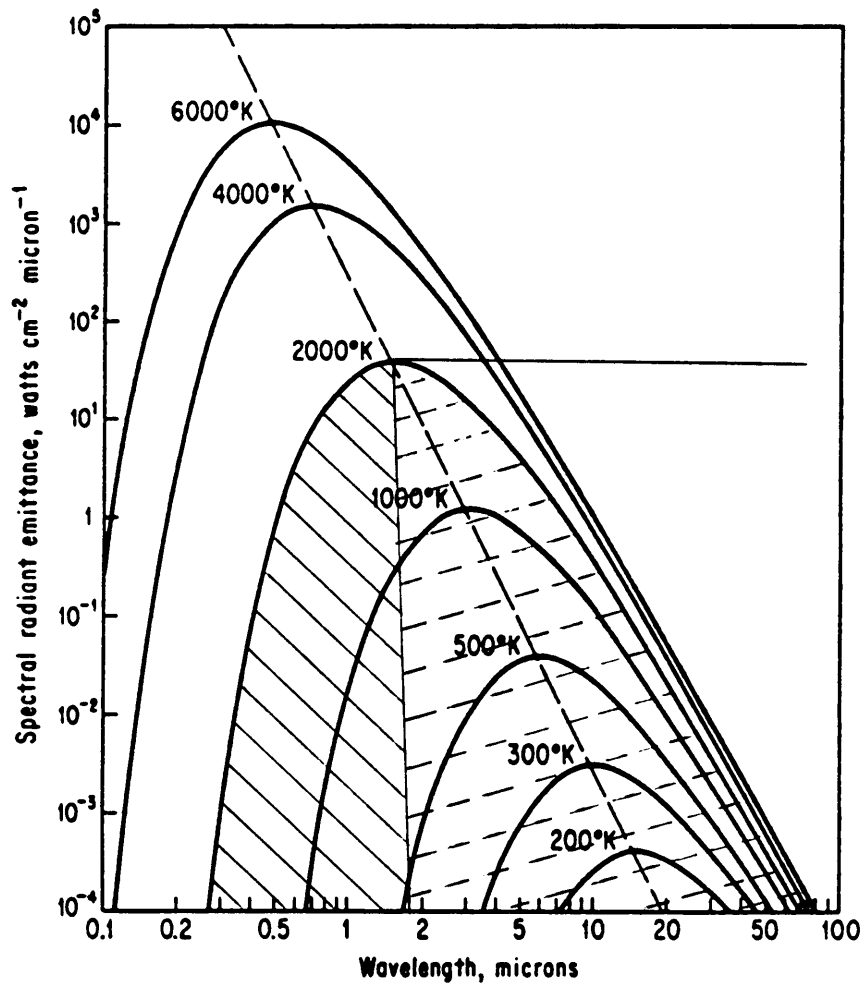
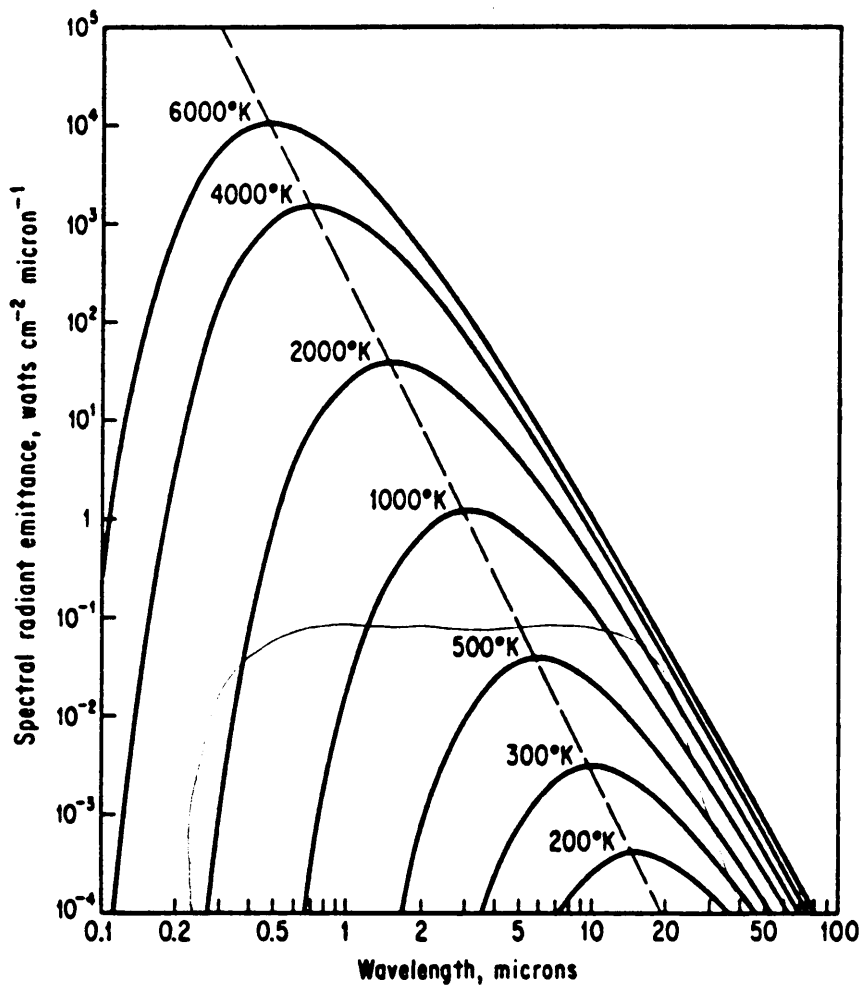


Figure 22. Filter Options: (a) 2 Wavelength pyrometry



b

Figure 23. Filter Options: (b) High and Low Pass Filters



c

Figure 24. Filter Options: (c) Responsivity

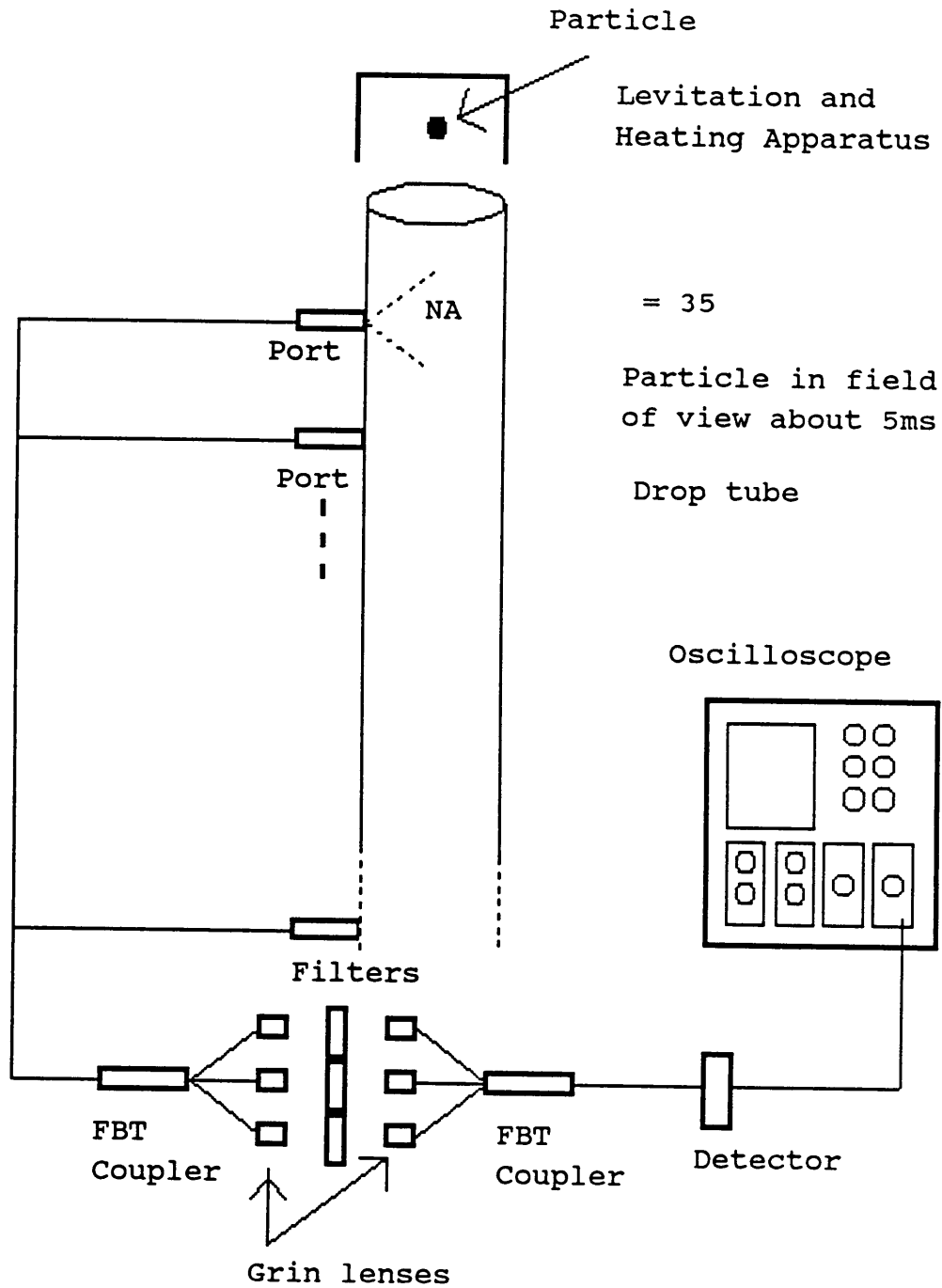


Figure 25. Drop Tube Instrumentation: An in-line optical fiber filtering function feeds a single optical detector.

where  $S(\lambda)$  shows the dependence of the output signal amplitude on wavelength,  $W(\lambda)$  is the optical power collected at the port,  $T(\lambda)$  accounts for the wavelength dependence of power through the fiber and all devices,  $R(\lambda)$  is the responsivity of the detector vs. wavelength, and  $F(\lambda)$  is the in-line filter function response. In equation (5-14),  $S(\lambda)$ ,  $W(\lambda)$ ,  $T(\lambda)$ ,  $R(\lambda)$ , and  $F(\lambda)$  should be interpreted as transfer functions of different modules in a block diagram representation of the system. Similarly, for the multi-wavelength system,

$$S_{\Sigma}(\lambda) = \sum_i W(\lambda) * T_i(\lambda) * R(\lambda) * F_i(\lambda), \quad (5-15)$$

where  $i$  counts all fiber/filter paths in the system.

The approach is to attempt a proof-of-concept experiment using available components to demonstrate the validity of this approach.

An experimental set-up is shown in Figure 26. The lamp (and its control unit) from the Zeiss microscope was placed approximately 0.75 m in front of two fiber optic power meters, each having a filter in front of it. One filter passed everything above 500 nm, and the other passed everything after 950 nm. The purpose of this was to see if the filtering ideas were feasible without fibers, and then use fibers only if the straight detectors worked.

Note on the blackbody curves that as temperature is increased, more power is shifted to shorter wavelengths. If the demonstration was to work, we should have been able to see more of the optical output at the meter with the 500 nm filter in front of it.

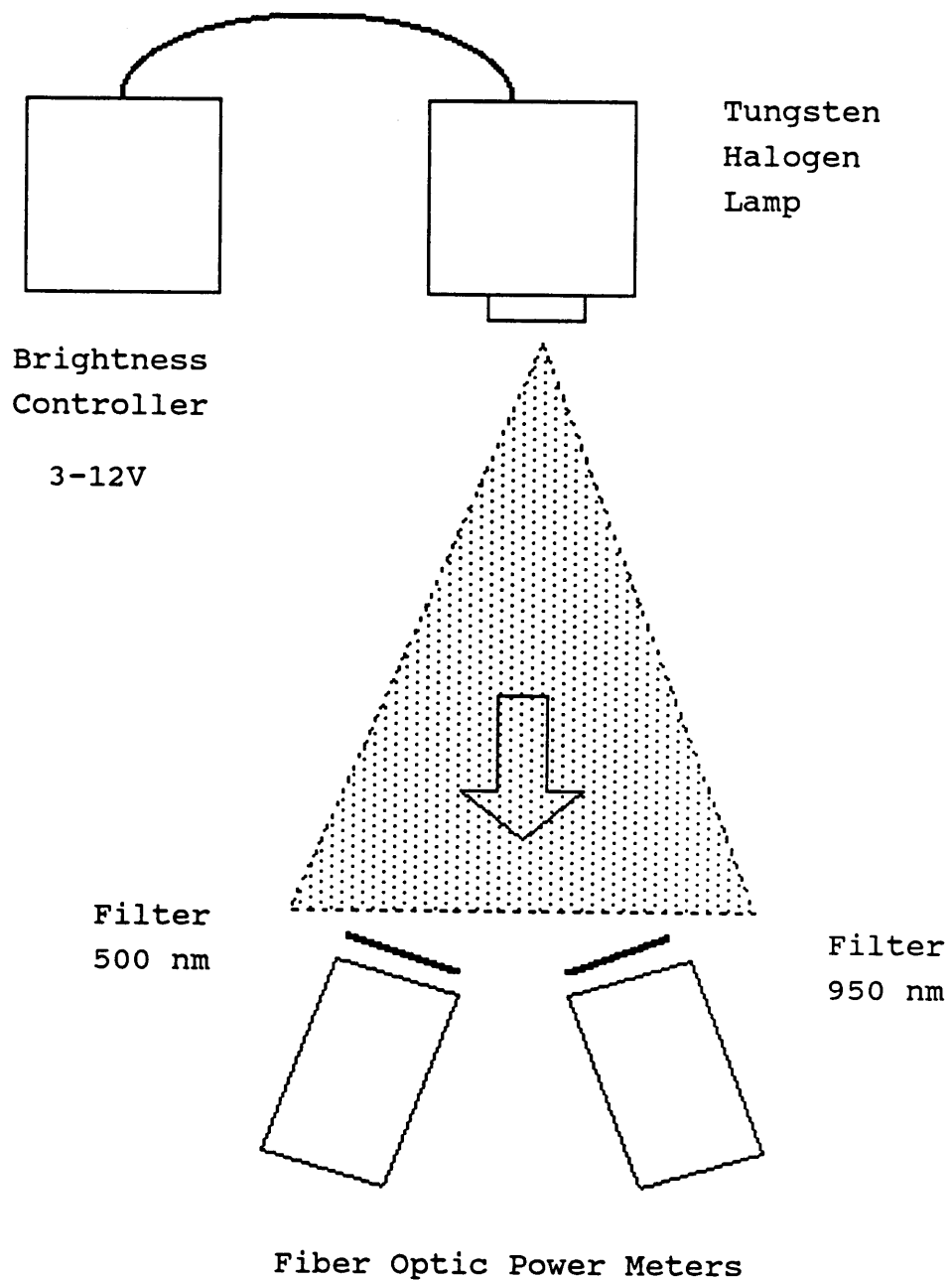


Figure 26. Experimental Set-up

Figures 27, 28, and 29 show the data collected. Indeed, as the voltage across the bulb was increased, more power was seen at shorter wavelengths.

# Trial 1

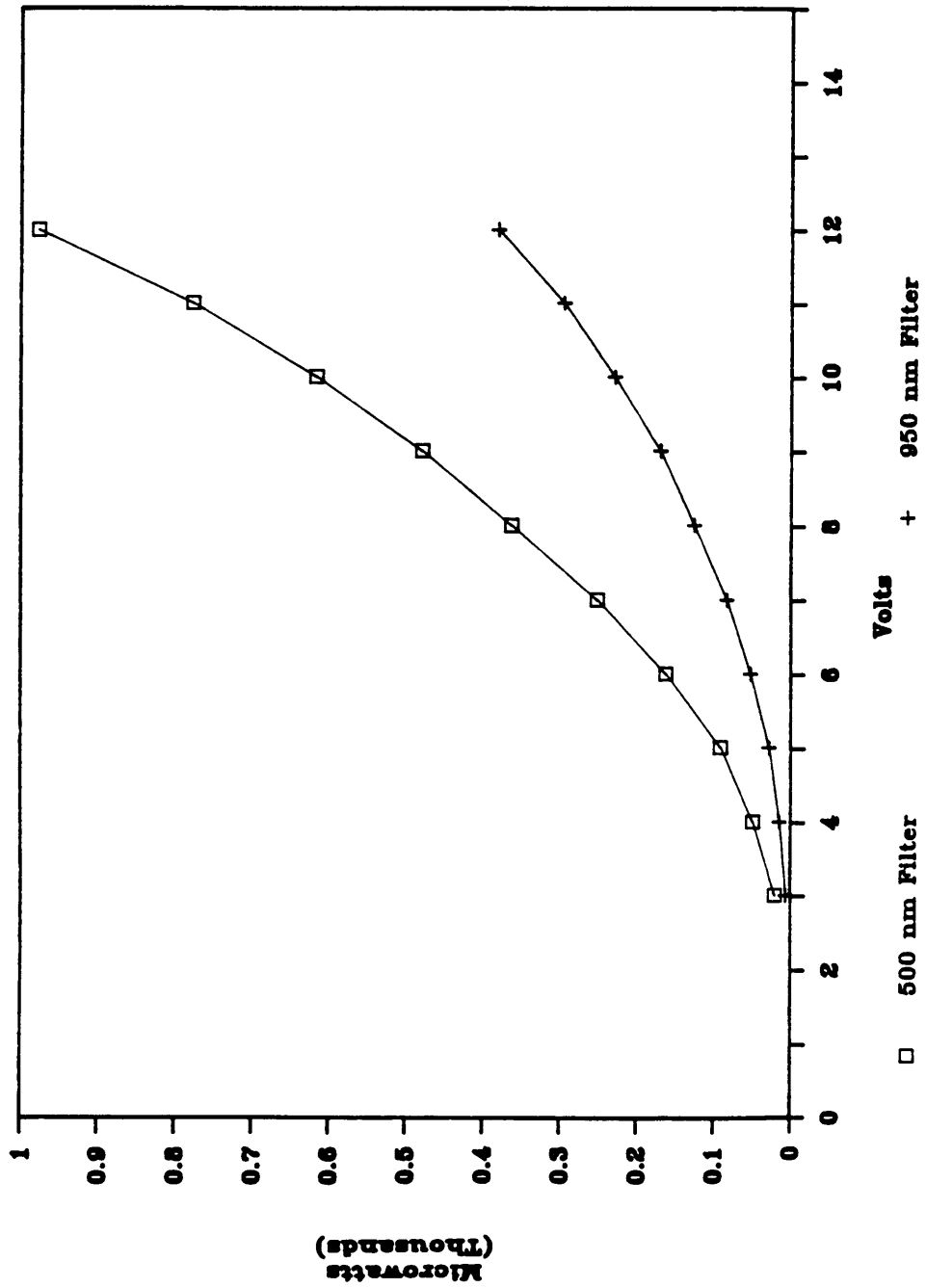


Figure 27. Power Collected, First Trial

# Trial 2

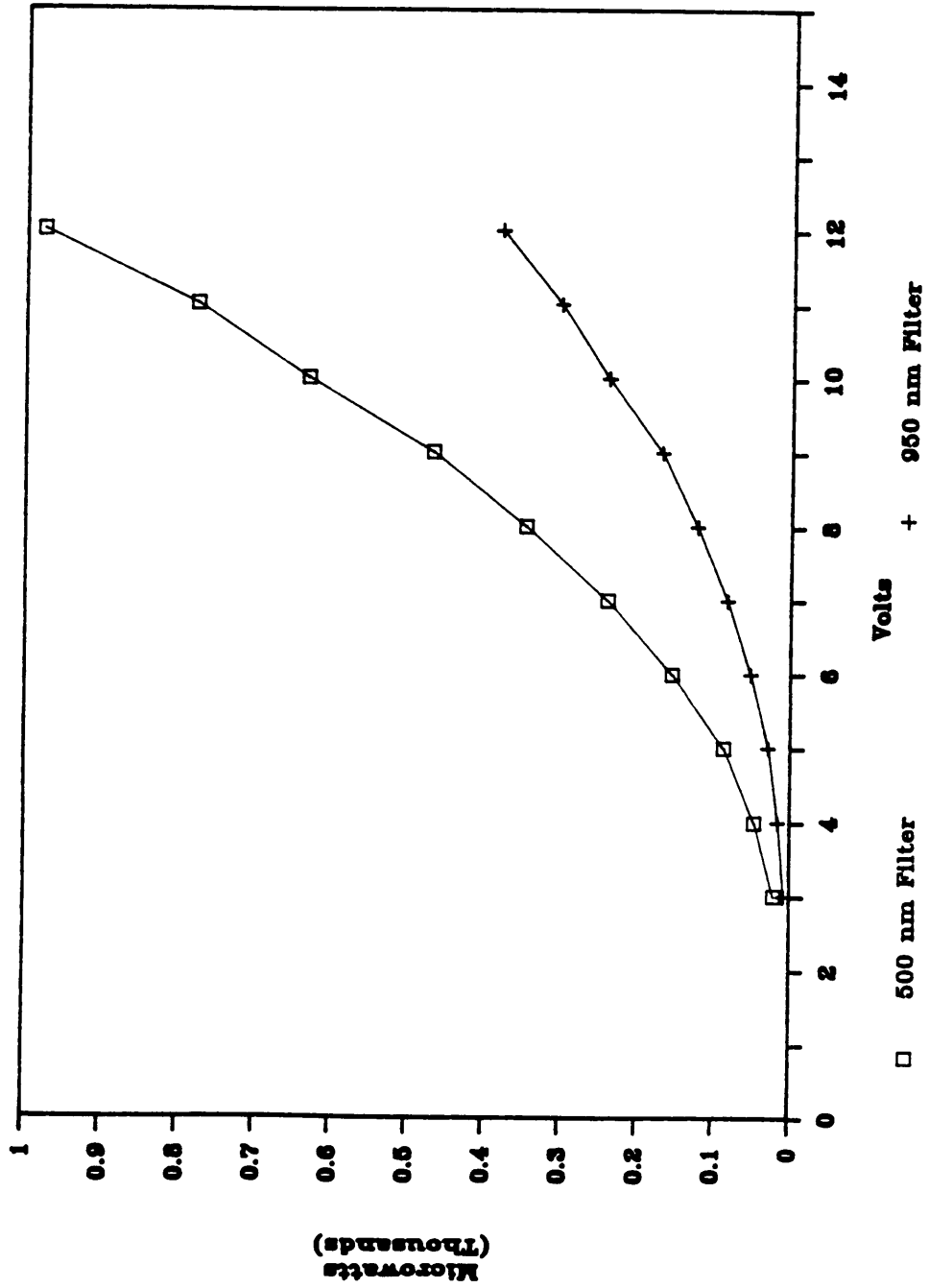


Figure 28. Power Collected, Second Trial

# Volts vs. $P(500)/P(950)$

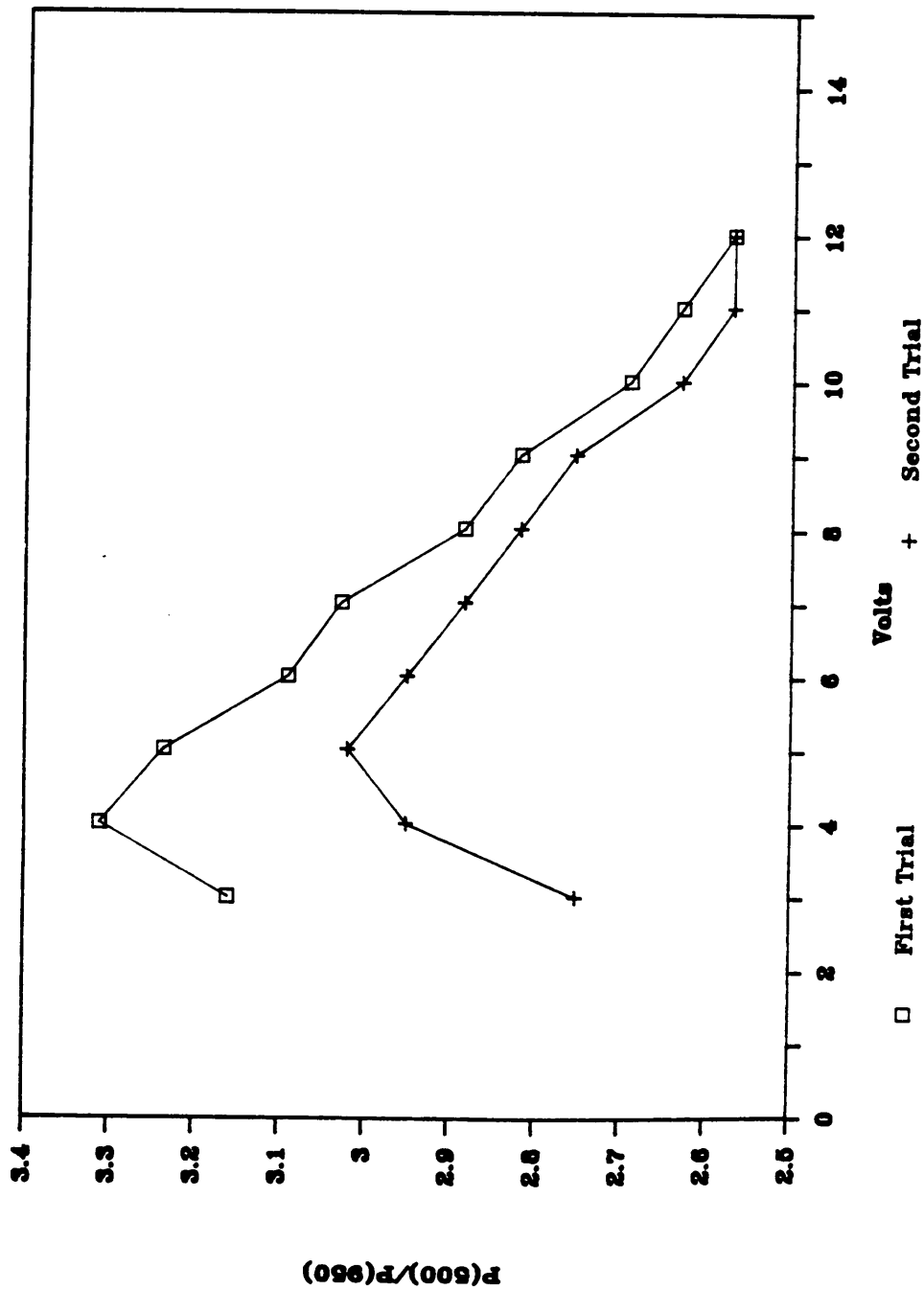


Figure 29. Ratio of Power Collected, First and Second Trials

## 6.0 Future Work and Conclusions

### 6.1 *Future Work*

The next step is to implement the fibers; probably fluoride, perhaps sapphire. If it turns out that our choice of filters is not a unique function of temperature, it may very well be that some other combination of filters will be. Perhaps even three filtering functions will be necessary. This is the crux of the problem: finding the appropriate filtering function to give us results that are a single valued function of temperature.

Following that, a blackbody simulator will be instrumented.

Several foreseeable problems exist. One will be capturing the light in the fiber as the particle falls past the port. The particle will only be in the field of view of the fiber for several milliseconds; and even though the fiber is small in comparison to the particle, the amount of power actually coupled into the fiber will be very small. Fast electronics will be required in order to take measurements at several points along the tube. The

wavelength-dependent attenuation of the fiber must be accounted for, as must the reflective properties of the drop tube.

Once the laboratory proof-of-principle is operational, a system can be fabricated and installed on a drop tube. If suitable electronics are found, a multi-port system can be implemented. It will be capable of determining the temperature of the particle at several instants in time as it travels all the way down the tube.

The radiometric method for determining temperature involves a measurement of the radiance from the target surface and a relationship to infer the temperature from the radiation measurement [55]. We need a method of converting our data into temperatures. Some sort of "look-up" table must be devised.

## ***6.2 Conclusions***

Nonsilica-based infrared optical fibers and their methods of fabrication have been thoroughly discussed. Here at Virginia Tech, some of the fabrication methods reviewed in this thesis may be considered for the manufacture of infrared fibers.

Several temperature sensing schemes using optical fibers have been described. We identified a problem that could utilize infrared fibers; the measurement of the temperature of a particle of a molten alloy as it falls down a drop tube. A ratio pyrometer approach is appropriate since temperature can be determined without knowledge of the emissivity of the material. The theory of pyrometry was therefore presented. Infrared fibers will allow the practical instrumentation of multi-wavelength

pyrometers well into the infrared. I set up a system with available components to demonstrate this approach. The measurements reported here demonstrate a proof-of-concept.

## References

1. Shibata, S., Horiguchi, M., Jinguji, K., Mitachi, S., Kanamori, T., Manabe, T., "Prediction of Loss Minima in Infra-Red Optical Fibers," *Electronics Letters*, Vol. 17, No. 21, 775, 15 October, 1981.
2. Culshaw, B., *Optical Fibre Sensing and Signal Processing*, Peter Peregrinus Ltd., London, 1984.
3. Marcuse, D., *Principles of Optical Fiber Measurements*, Academic Press, New York, 1981.
4. Keiser, G., *Optical Fiber Communications*, McGraw-Hill Book Company, New York, 1983.
5. Miyashita, T., Manabe, T., "Infrared Optical Fibers," *IEEE Journal of Quantum Electronics*, Vol. QE-18, No. 10, 10 October, 1982.
6. *Designers Guide to Fiber Optics*, AMP Incorporated, Harrisburg, PA, 1982.
7. Snyder, A. W., Love, J. D., *Optical Waveguide Theory*, Chapman and Hall, New York, 1983.
8. Cherin, A. H., *An Introduction to Optical Fibers*, McGraw-Hill Book Company, New York, 1983.
9. Jablonowski, D. P., "Fiber Manufacture at AT&T with the MCVD Process," *Journal of Lightwave Technology*, Vol. LT-4, No. 8, 1016, August, 1986.
10. Lydtin, H., "PCVD: A Technique Suitable for Large-Scale Fabrication of Optical Fibers," *Journal of Lightwave Technology*, Vol. LT-4, No. 8, 1034, August, 1986.

11. Lucas, J., "Infrared Fibers," *Infrared Physics*, Vol. 25, 277, 1985.
12. Savage, J. A., *Infrared Optical Materials and their Antireflection Coatings*, Adam Hilger Ltd., Bristol, 1985.
13. Poulain, M., Chanthanasinh, M., Lucas, J., "Nouveaux Verres Fluores," *Mat. Res. Bul.*, Vol. 12, 151, 1977.
14. Lucas, J., Fonteneau, G., Bouaggad, A., Hua, Z. X., "Two new families of halide glasses for infrared transmission," *New Materials for Optical Waveguides*, Proc. SPIE 799, 101, 1987.
15. Sakaguchi, S., Takahashi, S., "Low-Loss Fluoride Optical Fibers for Midinfrared Optical Communication," *Journal of Lightwave Technology*, Vol. LT-5, No. 9, 1219, September, 1987.
16. Bansal, N. P., Bruce, A. J., Doremus, R. H., Moynihan, C. T., "Crystallization of heavy metal fluoride glasses," *Infrared Optical Materials and Fibers III*, Proc. SPIE 484, 51, 1984.
17. Takahashi, H., Sugimoto, I., "A Germanium-Oxide Glass Optical Fiber Prepared by a VAD-Method," *Journal of Lightwave Technology*, Vol. LT-2, No. 5, 613, October, 1984.
18. McEnroe, D. J., Finney, M. J., Prideaux, P. H., Schultz, P. C., "The strength of infrared transmitting optical fibers," *New Materials for Optical Waveguides*, Proc. SPIE 799, 39, 1987.
19. Pitt, N. J., "Loss mechanisms in chalcogenide glass optical fibers," *New Materials for Optical Waveguides*, Proc. SPIE 799, 25, 1987.
20. Mitachi, S., Ohishi, Y., Miyashita, T., "A Fluoride Glass Optical Fiber Operating in the Mid-Infrared Wavelength Range," *Journal of Lightwave Technology*, Vol. LT-4, No. 1, 67, March, 1983.
21. Tran, D. C., Fischer, C. F., Sigel, G. H., "Fluoride Glass Preforms by a Rotational Casting Process," *Electronics Letters*, Vol. 18, No. 15, 657, 22 July, 1982.
22. Ohishi, Y., Mitachi, S., Takahashi, S., "Fabrication of Fluoride Glass Single-Mode Fibers," *Journal of Lightwave Technology*, Vol. LT-2, No. 5, 593, October, 1984.
23. Tran, D. C., Sigel, G. H., Bendow, B., "Heavy Metal Fluoride Glasses and Fibers: A Review," *Journal of Lightwave Technology*, Vol. LT-2, No. 5, 566, October, 1984.
24. Kanamori, T., Terunuma, Y., Takahashi, S., Miyashita, T., "Chalcogenide Glass Fibers for Mid-Infrared Transmission," *Journal of Lightwave Technology*, Vol. LT-2, No. 5, 607, October, 1984.

25. Bridges, T. J., Hasiak, J. S., Strnad, A. R., "Single-crystal AgBr infrared optical fibers," *Optics Letters*, Vol. 5, No. 3, 85, March, 1980.
26. Saito, M., Takizawa, M., Miyagi, M., "Optical and Mechanical Properties of Infrared Fibers," *Journal of Lightwave Technology*, Vol. 6, No. 2, 233, February, 1988.
27. Walker, K. L., Broer, M. M., Carnevale, A., "Dispersion Shifted Fiber Designs with Low Bending Losses for Infrared Materials," *Infrared and Optical Materials and Fibers IV*, Proc. SPIE 618, 17, 1986.
28. Panel Discussion, "The Future in Infrared Fibers," *Advances in Infrared Fibers II*, Proc. SPIE 320, 148, 1982.
29. Artyushenko, V. G., Butvina, L. N., Voitsekhovskii, V. V., Dianov, E. M., Kuznetsov, R. I., Sysoev, V. K., "Use of IR optical fibers for temperature-monitoring systems," *Sov. Tech. Phys. Lett.*, Vol. 10, No. 6, 310, June, 1984.
30. Rochereau, J., "High temperature measurements with a fiber optic pyrometric sensor," *Fiber Optic Sensors*, Proc. SPIE 586, 178, 1985.
31. Zur, A., Katzir, A., "Use of infrared fibers for low-temperature radiometric measurements," *Applied Physics Letters*, Vol. 48, No. 7, 499, 17 February, 1986.
32. Mordon, S., Zoude, E., Brunetaud, J. M., "Non-Contact Temperature Measurement with a Zirconium Fluoride Glass Fiber," *Optical Fiber Sensors, 1988 Technical Digest Series*, Vol. 2, Optical Society of America, Washington, D. C., 502, January, 1988.
33. Grattan, K. T. V., Palmer, A. W., "Infrared fluorescence 'decay-time' temperature sensor," *Rev. Sci. Instrum.*, Vol. 56, No. 9, 1784, September, 1985.
34. Giallorenzi, T. G., Bucaro, J. A., Dandridge, A., Sigel, G. H., Cole, J. H., Rashleigh, S. C., Priest, R. G., "Optical Fiber Sensor Technology," *IEEE Journal of Quantum Electronics*, Vol. QE-18, No. 4, 626, April, 1982.
35. Hocker, G. B., "Fiber-optic sensing of pressure and temperature," *Applied Optics*, Vol. 18, No. 9, 1445, 1 May, 1979.
36. Tseng, S. M., Chen, C. L., "Optical fiber Fabry-Perot sensors," *Applied Optics*, Vol. 27, No. 3, 547, 1 February, 1988.
37. Eickhoff, W., "Temperature sensing by mode-mode interference in birefringent optical fibers," *Optics Letters*, Vol. 6, No. 4, 204, April, 1981.
38. Kawata, S., Shigeoka, T., Okamoto, T., Minami, S., "Heterodyne Interferometric Temperature Sensor Using a Transverse Zeeman Laser and a Polarization Maintaining Fiber," *Fiber Optic and Laser Sensors III*, Proc. SPIE 566, 307, 1985.

39. Corke, M., Kersey, A. D., Jackson, D. A., "Temperature sensing with single-mode optical fibres," *J. Phys. E: Sci. Instrum.*, Vol. 17, 988, 1984.
40. Martinelli, M., "Unlimited phase compensator for fiber-optic interferometric detection of slow temperature change," *Optics Letters*, Vol. 9, No. 9, 429, September, 1984.
41. McMillan, J. L., Robertson, S. C., "Dual-Mode Optical-Fibre Interferometric Sensor," *Electronics Letters*, Vol. 20, No. 3, 136, 2 February, 1984.
42. Leilabady, P. A., Jones, J. D. C., Corke, M., "A dual interferometer implemented in parallel on a single birefringent monomode optical fibre," *J. Phys. E: Sci. Instrum.*, Vol. 19, 143, 1986.
43. Meltz, G., Dunphy, J. R., Morey, W. W., Snitzer, E., "Cross-talk fiber-optic temperature sensor," *Applied Optics*, Vol. 22, No. 3, 464, 1 February, 1983.
44. Grattan, K. T. V., Palmer, A. W., Selli, R. K., "Doped Glass Absorption Thermometer with Fluorescent Referencing," *Fiber Optic and Laser Sensors III*, Proc. SPIE 566, 333, 1985.
45. Falco, L., Berthou, H., Cochet, F., Scheja, B., Parriaux, O., "Temperature sensor using single mode fiber evanescent field absorption," *Fiber Optic Sensors*, Proc. SPIE 586, 114, 1985.
46. Hartog, A. H., "A Distributed Temperature Sensor Based on Liquid-Core Optical Fibers," *Journal of Lightwave Technology*, Vol. LT-1, No. 3, 498, September, 1983.
47. Dakin, J. P., Pratt, D. J., Bibby, G. W., Ross, J. N., "Temperature Distribution Measurement Using Raman Ratio Thermometry," *Fiber Optic and Laser Sensors III*, Proc. SPIE 566, 249, 1985.
48. Dakin, J. P., Pratt, D. J., Bibby, G. W., Ross, J. N., "Distributed Optical Fibre Temperature Sensor Using a Semiconductor Light Source and Detector," *Electronics Letters*, Vol. 21, No. 13, 569, 20 June, 1985.
49. Farries, M. C., "Spontaneous Raman temperature sensor," *Fiber Optic Sensors*, Proc. SPIE 586, 120, 1985.
50. Legendre, J. P., "A simple reflectometer configured to sense temperature," *Fiber Optic and Laser Sensors III*, Proc. SPIE 566, 321, 1985.
51. Doebelin, E. O., *Measurement Systems, Application and Design*, McGraw-Hill Book Company, New York, 1983.
52. Jamieson, J. A., McFee, R. H., Plass, G. N., Grube, R. H., Richards, R. G., *Infrared Physics and Engineering*, McGraw-Hill Book Company, New York, 1963.

53. Wyatt, C. L., *Radiometric System Design*, Macmillan Publishing Company, New York, 1987.
54. Jorgensen, F. R. A., Zuiderwyk, M., "Two-colour pyrometer measurement of the temperature of individual combusting particles," *J. Phys. E: Sci. Instrum.*, Vol. 18, 486, 1985.
55. DeWitt, D. P., "Principles of Calibration for Radiometric Temperature Measurements," *Thermosense VII*, Proc. SPIE 520, 2, 1984.

**The vita has been removed from  
the scanned document**